ANL-HEP-TR--92-74

DE93 005550

UNIVERSITY OF CALIFORNIA

Los Angeles

A High Current, Short Pulse Electron Source for Wakefield Accelerators *

A dissertation submitted in partial satisfaction of the
requirements for the degree Doctor of Philosophy
in Physics

by

Ching-Hung Ho

1992

---

*This work supported by the U.S. Department of Energy, Division of High Energy Physics, under Contract W-31-109-ENG-38.

The dissertation of Ching-Hung Ho is approved.

John M. Dawson

John M. Dawson

N. C. Luhmann, Jr.

Mark Morris

Mark Morris

Claudio Pellegrini

James D. Simpson

James D. Simpson

David B. Cline, Committee Chair

University of California, Los Angeles

1992

DEDICATION

To my wife Victoria Huey-Ling Ho, my daughter Jennifer S. Ho, my grandparents, my parents, my brothers and sisters, and all the friends and colleagues who helped.

Contents

List of Figures

List of Tables

ACKNOWLEDGEMENTS

I would like to thank my advisor, Prof. David Cline, for steering me into the field of accelerator physics and for his constant inspiration. I treasure friendships with all the people I met at the UCLA Physics Department. In particular, I am indebted to Yentang Oyang for his encouragement when I was in low spirits.

This work has been performed with the advanced accelerator group in the High Energy Physics Division of Argonne National Laboratory. It has really been a precious experience for me to participate in the Argonne Wakefield Accelerator project since its onset. I would like to acknowledge valuable advice and help from Paul Schoessow in particle simulations, Eric Chojnacki in rf engineering and Wei Gai in wakefield calculations. I would also like to extend my gratitude to other members of this group, which includes Dick Konecny, Jim Norem, John Power and Mike Rosing, for stimulating discussions and various assistances. I cannot begin to express my deepest thanks to Jim Simpson, who initiated this unique opportunity and has provided steady support throughout. The hospitality of the High Energy Physics Division has also made my stay at Argonne very enjoyable.

The financial support from the US Department of Energy, Division of High Energy Physics, is gratefully acknowledged. I also appreciate the opportunity to carry out this thesis project as a Laboratory Graduate at Argonne National Laboratory through its Division of Education Programs.

Last, but not the least, I would like to thank my wife, Victoria Huey-Ling Ho, and all of my family for their love and constant support.

VITA

May 28,1957	Born, Taiwan, Republic of China
1979	B.S., Physics National Tsing Hua University Taiwan, Republic of China
1981-1982	Research Assistant National Tsing Hua University Taiwan, Republic of China
1983-1984	Teaching Assistant Wayne State University Detroit, Michigan
1984	M.S., Physics Wayne State University Detroit, Michigan
1984-1988	Teaching Assistant Department of Physics University of California, Los Angeles
1988-1992	Laboratory Graduate Argonne National Laboratory Argonne, Illinois

PUBLICATIONS AND PRESENTATIONS

1. Gai, W., and Ho, C. H., "Modelling of the Transverse Mode Suppressor for Dielectric Wake-Field Accelerator," J. Appl. Phys. **70**, 3955 (1991).
2. Ho, C. H., "AWA RF Photocathode Design," Bull. Am. Phys. Soc. **35**, 956 (1990).
3. Schoessow, P., and Ho, C. H. *et al.*, "The Argonne Wakefield Accelerator," in *Proc. 2nd European Particle Accelerator Conf.* (Nice, France, 1990), p. 606.

ABSTRACT OF THE DISSERTATION

A High Current, Short Pulse Electron Source for Wakefield Accelerators

by

Ching-Hung Ho
Doctor of Philosophy in Physics
University of California, Los Angeles, 1992
Professor David B. Cline, Chair

Design studies for the generation of a high current, short pulse electron source for the Argonne Wakefield Accelerator are presented. An L-band laser photocathode rf gun cavity is designed using the computer code URMEL to maximize the electric field on the cathode surface for fixed frequency and rf input power. A new technique using a curved incoming laser wavefront to minimize the space charge effect near the photocathode is studied. A preaccelerator with large iris to minimize wakefield effects is used to boost the drive beam to a useful energy of around 20 MeV for wakefield acceleration experiments. Focusing in the photocathode gun and the preaccelerator is accomplished with solenoids. Beam dynamics simulations throughout the preaccelerator are performed using particle simulation codes TBCI-SF and PARMELA. An example providing a useful set of operation parameters for the Argonne Wakefield Accelerator is given. The effects of the sagitta of the curved beam and laser amplitude and timing jitter effects are discussed. Measurement results of low rf power level bench tests and a high power test for the gun cavity are presented and discussed.

1 Introduction

The significance of particle accelerators in high energy physics research is described. The demands for new methods of acceleration in order to build more powerful high energy accelerators are examined. We then review the history of wakefield acceleration technology which is one of the most straightforward among various new acceleration schemes. We next discuss the need for a high current, short pulse electron source for wakefield accelerators, which motivated the research described herein. An outline for the remainder of the thesis concludes this chapter.

1.1 THE FUTURE OF HIGH ENERGY ACCELERATORS

High energy accelerators are essential tools for particle physicists to probe the elementary structure of matter, the fundamental forces of nature and the entire evolution of the universe. These questions are among deepest mysteries humans have tried to understand since the earliest times. The prevailing answers to these questions have changed as we learned more and more. Much of this has been possible because the center-of-mass energies available at accelerators have grown exponentially over the past fifty years due to timely inventions of new devices and breakthroughs in technology. At present all types of accelerators have found wide applications in industry, condensed matter, materials science, medical diagnosis and treatment, nuclear physics and many other basic research sciences.

Historically, the picture of the basic building blocks of matter has evolved as the atom, the nucleus, the nucleon, and now the nucleon's constituents (the quarks). Theoretical and experimental breakthroughs in the past several decades led to the establishment of the so called Standard Model. This model speculates that there are two basic categories of particles: the matter particles which consist of the three generations of quarks and leptons, and the force particles (also known as gauge particles) which are photons, W's, Z's and gluons. So far, the Standard Model is able to explain all the phenomena observed in high-energy laboratories around the world. Along the way to this tremendous accomplishment, we have progressed through Cockcroft-Walton generators, Van de Graaff machines, cyclotrons, betatrons, synchrotrons, strong focusing machines, linacs, storage rings and colliders. Yet this is not the end of story. Many people feel the Standard Model is not the final answer for several reasons. One of the main difficulties is the picture requires about twenty parameters (coupling constants, masses and mixing angles) to be specified, and many physicists believe this is too many for a fundamental theory. Another reason is that this model gives answers contradictory to accepted conservation laws when it is applied to much higher energy regimes than what are experimentally accessible at present.

To continue the tour of uncovering the nature's secrets, we need more powerful accelerators. However, the cost and size of the accelerators has already increased to the point where it is becoming impractical to build machines much larger than the Superconducting Super Collider (SSC) with conventional technologies. Synchrotron radiation losses and the technical difficulty of constructing magnets with fields greater than 8 Tesla impose the ultimate limit on the size of circular machines. Thus linear colliders are considered to be better candidates for the next generation (post-SSC) of high energy accelerators. But a linear accelerator using the SLAC accelerating gradient of around 20 MV/m would be so long that the cost and alignment problems become insurmountable. There are several new methods proposed to achieve high gradient acceleration. Wakefield acceleration is one of the more promising schemes for a future high energy accelerator. The historical perspective on wakefield accelerators is presented in the next section.

1.2 REVIEW OF WAKEFIELD ACCELERATORS

The concept of wakefield acceleration can be traced back tc as early as the 1950s,[1,2] but it was not taken seriously until the 1980s when people began to look at novel schemes of acceleration for the next generation collider. The principle of wakefield accelerators is simple. Just as a boat moving through water leaves behind a wake, so a bunch of charged particles passing through specific media excites electromagnetic fields, called wakefields, via the interaction with its surroundings. By proper arrangements, the wakefield left behind an initial bunch of particles (the driver beam) can be used to accelerate a trailing bunch of particles (the witness beam). It's similar to a surfer riding the wave caused by the wake of a speedboat.

If both beams are at relativistic velocities, the difference in velocities results in only a long time-scale phase slip. In some sense, wakefield acceleration is only a step away from conventional rf acceleration in which the rf energy generated by a low energy beam in an rf cavity of a klystron is extracted to a separate rf accelerating cavity, whereas both driver and witness beams use the same rf cavity in the wakefield acceleration. Wakefield technology, however, can potentially provide ten to one hundred times higher accelerating gradients than are available in conventional machines.

Wakefield accelerators can be classified according to their use of different wakefield devices. Several devices such as iris-loaded cavities,[3,4] plasmas,[5-7] and dielectric structures,[8,9] have been proposed during the past decade. But we could not experimentally scrutinize and compare different wakefield schemes until commissioning of the Advanced Accelerator Test Facility (AATF)[10,11] at Argonne National Laboratory in 1987. This facility has enabled direct measurement of wakefields for the first time ever. A schematic of the AATF is illustrated in Fig. 1.2.1. The detailed description and the operational characteristics of the AATF can be found in Ref. 12. AATF experiments have investigated all three types of wakefield devices mentioned above.

The device, named the Wakeatron,[3] proposed to use a sequence of iris-coupled cylindrical rf cavities, similar to a traditional linac accelerating structure, as the wakefield device. As the beam travels through the device, electromagnetic fields, which act back on the particles, will be excited through the interaction between the beam and the structure. Agreement between the experimental result[12] and the well understood theory of this device validated the AATF performance.

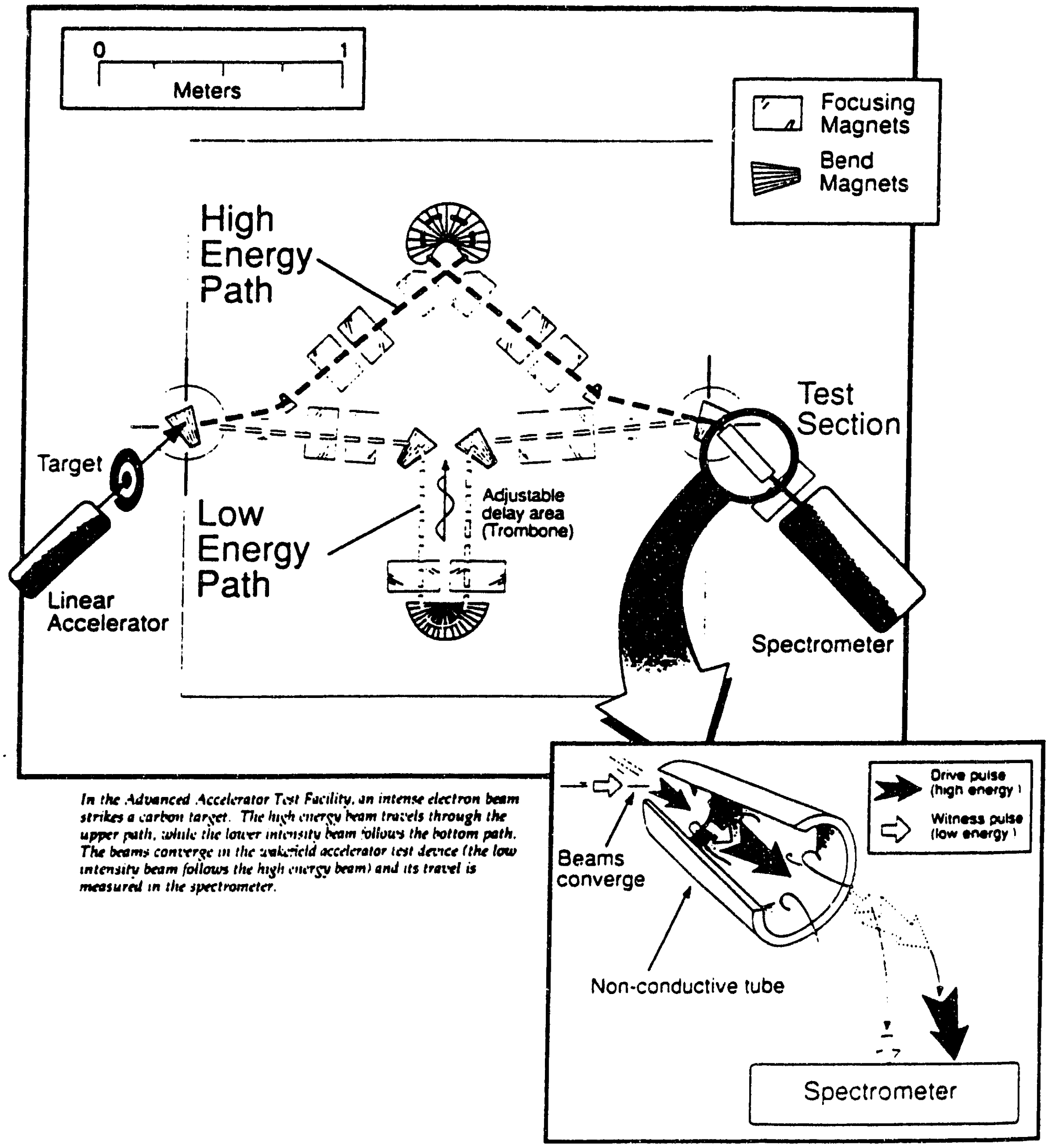

In the Advanced Accelerator Test Facility, an intense electron beam strikes a carbon target. The high energy beam travels through the upper path, while the lower intensity beam follows the bottom path. The beams converge in the wakefield accelerator test device (the low intensity beam follows the high energy beam) and its travel is measured in the spectrometer.

Figure 1.2.1: Schematic drawing of the Advanced Accelerator Test Facility.

The plasma wakefield accelerator uses a column of plasma, which is a state of matter heated to a temperature high enough to dissociate the gas atoms into electrons and ions, as the wakefield device. The physical mechanism of the plasma wakefield accelerator is well explained in Ref. 13. When the electron beam enters the plasma, it creates regions of negative charge (high concentrations of electrons) and regions of positive charge (high concentrations of positive ions) and thus sets up an electric field which runs from positive to negative regions. This electric field will pull plasma electrons toward the almost immobile, massive ions. The plasma electrons overshoot due to their inertia and oscillate like a pendulum, in the direction parallel to the beam velocity. An array of such electron pendulums along the plasma column will then establish an electric field to accelerate a properly injected trailing beam. The plasma acceleration schemes have attracted considerable attention in the past several years mostly because of the possibility of achieving an ultrahigh accelerating gradient of the order of several GV/m. The plasma, which has already been ionized, is immune from electric field breakdown limitations and can thus sustain such a high gradient field. Associated with this longitudinal wakefield for acceleration, however, is also a transverse wakefield with comparable strength which can either focus or defocus the beam. Plasma lenses[14] take advantage of this strong self-focusing force of a beam traversing the plasma and may provide a new method for the final focus system at the interaction point in future colliders. However, in a wakefield configuration, the witness beam can be deflected out of the accelerator by this transverse wakefield if both drive and witness beams are not aligned precisely. Another problem of the plasma wakefield scheme is the difficulty in using external magnetic focusing to control the beam transport through the plasma. Interaction between the plasma electrons and the external magnetic field will alter the plasma to a possibly undesirable state for wakefield generation. Both the plasma wakefield acceleration[15,16] and the plasma focusing effect[17,18] were demonstrated for the first time at the AATF. Longitudinal wakefields around 5 MV/m were measured in these experiments.

The Cherenkov wakefield accelerator uses a hollow, cylindrical tube of dielectric material, such as ceramic or plastic, inserted into a pipe of good conductor as the wakefield device. When the electron beam passes through the dielectric tube, it generates a wakefield in the form of Cherenkov radiation due to the fact that the speed of light inside the insulating material is slower than that of the polarization charges induced by the beam. The Cherenkov wakefield scheme promises a high accelerating gradient of around 200 MV/m. The advantages of this scheme are the simplicity of the device, making it very easy to construct, and the ease of using external magnetic focusing to control beam transport without interference with wakefield generation. Again, experiments at the AATF found good agreement with theoretical and computational models.[19] Unfortunately the Cherenkov wakefield scheme also faces some problems of beam break up instabilities due to the transverse wakefield, although it has a smaller ratio of transverse to longitudinal wake amplitudes than wakeatrons or plasmas.[20,21] A recent simulation study shows that single bunch beam break up effects (head-tail instabilities) can be controlled to a certain degree by alternating focusing and defocusing quadrupole magnets applied around the wakefield tube.[22,23] Also a transverse modes suppressor in the dielectric structure to suppress multiple bunches beam break up was proposed and successfully tested recently.[24,25]

1.3 THE NEED FOR HIGH CURRENT BEAMS

As described in the last section, the principles of wakefield acceleration has been demonstrated in a series of AATF experiments. However, only modest accelerating gradients were observed due to the limited driving electron beam intensity and relatively long bunch length available at the AATF. The accelerating wakefield amplitude in a 20 GHz Cherenkov wakefield structure can exceed 2 MV/m for 1 nC of beam with delta function like bunch length. To achieve a higher accelerating gradient of 200 MV/m, we need about 100 nC of beam charge and about 10 ps of bunch length. The bunch length of the driving beam should be less than about a quarter period of the wakefield wavelength in order to avoid destructive interferences of accelerating wakefield amplitudes produced from all electrons in the driving bunch. Thus the bunch length of the driving beam should be around 10 ps for a 20 GHz wakefield structure. This demand of generating a high current, short pulse electron bunch thus motivates this thesis investigation. It is also the core of the phase-I of the Argonne Wakefield Accelerator (AWA) project,[26–28] which will serve as a demonstration accelerator using wakefield technology. A general overview of the AWA will be given later.

1.4 OUTLINE OF THE THESIS

The thesis will be organized as follows. In Chapter 2 we give an overview of the AWA, and then focus on the design of main components for the electron source. A systematic study and simulation results will be presented and discussed in Chapter 3. Several experimental investigations related to cavity measurements and a high power cavity test are presented in Chapter 4. Finally Chapter 5 is devoted to conclusions.

2 Design Studies

We first give an overview of the whole Argonne Wakefield Accelerator project. Then we'll focus on the design for each component of the 100 nC electron source. The design principle and several special techniques employed in the photocathode rf gun cavity are explained. The design goal and distinct features of the 20 MeV preaccelerator are studied. We also describe the AWA laser system, focusing elements, vacuum, diagnostics, and control system. A separate section is provided to explain the difference between the techniques used to generate witness beam at the AWA and the AATF.

2.1 OVERVIEW OF THE ARGONNE WAKEFIELD ACCELERATOR

Based on the success of proof-of-principle experiments conducted at the AATF, a new research facility, the Argonne Wakefield Accelerator, is under construction. Its goals are to develop wakefield related acceleration technology and to demonstrate a practical 1 GeV wakefield accelerator with an acceleration gradient of greater than 100 MV/m. A schematic layout of this new facility is shown in Fig. 2.1.1. The main components of the AWA consist of (1) an rf photocathode electron source producing short intense bunches, (2) a 20 MeV standing wave preaccelerator, (3) a drive linac system configured for heavy beam loading to accelerate the intense bunches to 150 MeV, (4) wakefield accelerator sections and staging to accelerate the witness beam to a final energy of 1 GeV. (1) and (2) constitute the phase-I of AWA and the emphasis of this thesis.

The front end of the AWA features a photocathode rf gun capable of producing 100 nC, 10 ps electron bunches and a standing wave preaccelerator to boost the beam energy to 20 MeV. The designs of the photocathode gun and the preaccelerator are the main topics of this chapter and will be investigated in subsequent sections. In addition to the gun and the preaccelerator, the first phase of the AWA will include a test section, spectrometer, and provisions for delayed witness beam generation to permit continuity of the AATF wakefield measurement program while at the same time extending its capabilities far beyond those available at the AATF. The area layout of phase-I of the AWA is shown in Fig. 2.1.2, while a block diagram showing main components is sketched in Fig. 2.1.3. An engineering drawing of the gun cavity and solenoids is shown in Fig. 2.1.4.

Unlike the AATF, where the witness beam is created by degrading a portion of the driver beam on a carbon target, the AWA will produce a 1 nC witness beam from a separate rf photocathode cavity. This is described later in detail in the witness gun section. The delays between the drive and the witness beam can be adjusted by the laser beam delay optics together with an rf phase shifter. This technique has the advantage of providing a much larger range of delays than the AATF. After passage through the test device, the longitudinal and transverse energy deviations of the witness beam as a function of its delay with respect to the driver bunch are measured by the magnetic spectrometer.

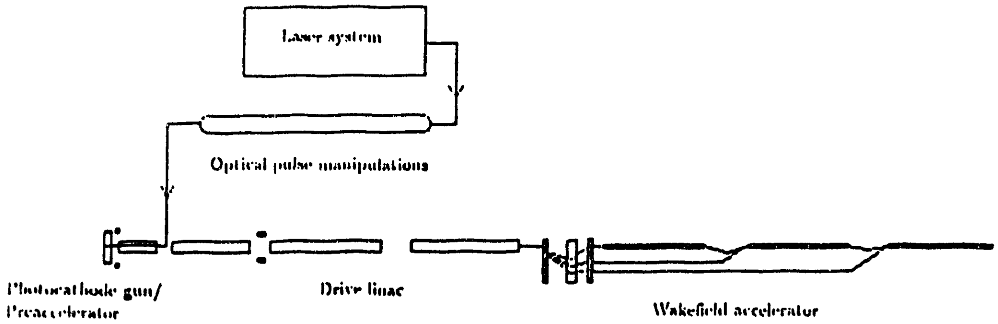

Figure 2.1.1: Schematic drawing of the Argonne Wakefield Accelerator facility.

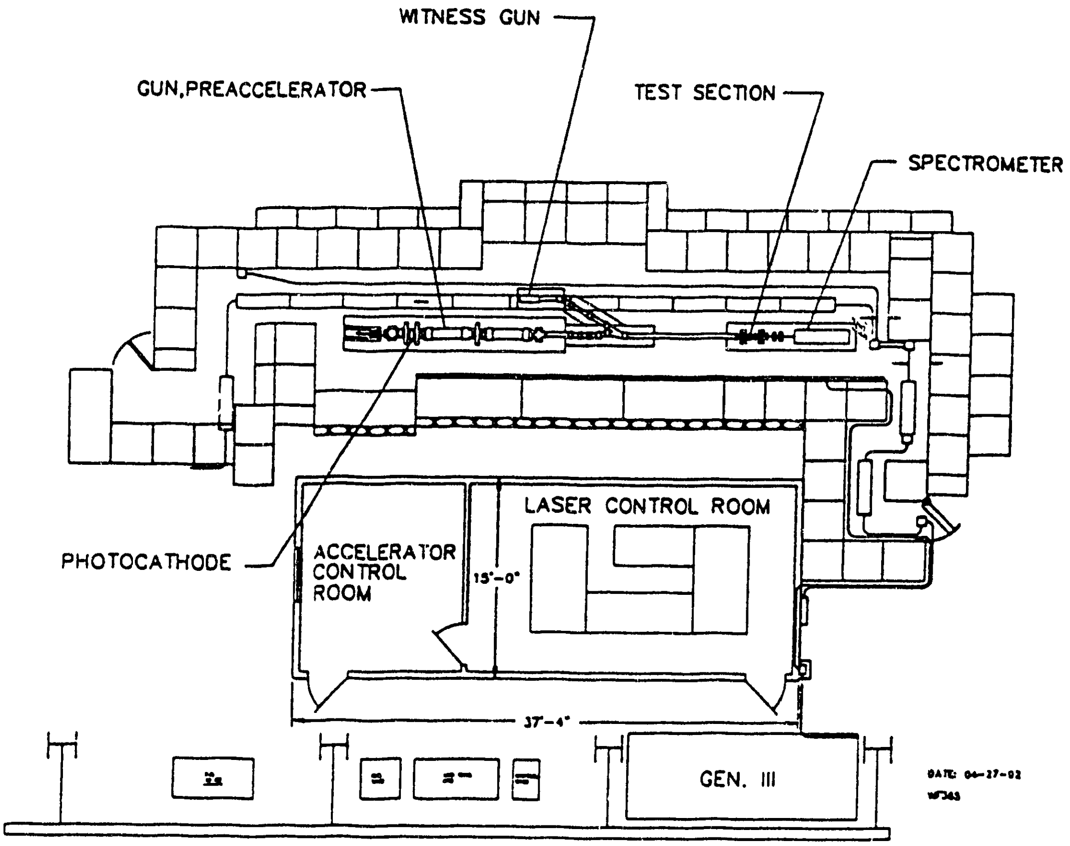

Figure 2.1.2: Area layout of phase-I of the AWA facility.

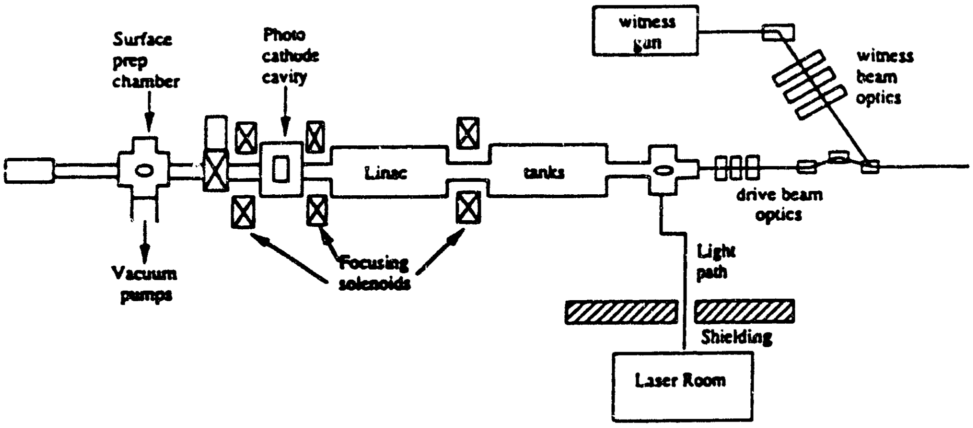

Figure 2.1.3: Block diagram showing main components of phase-I of the AWA facility.

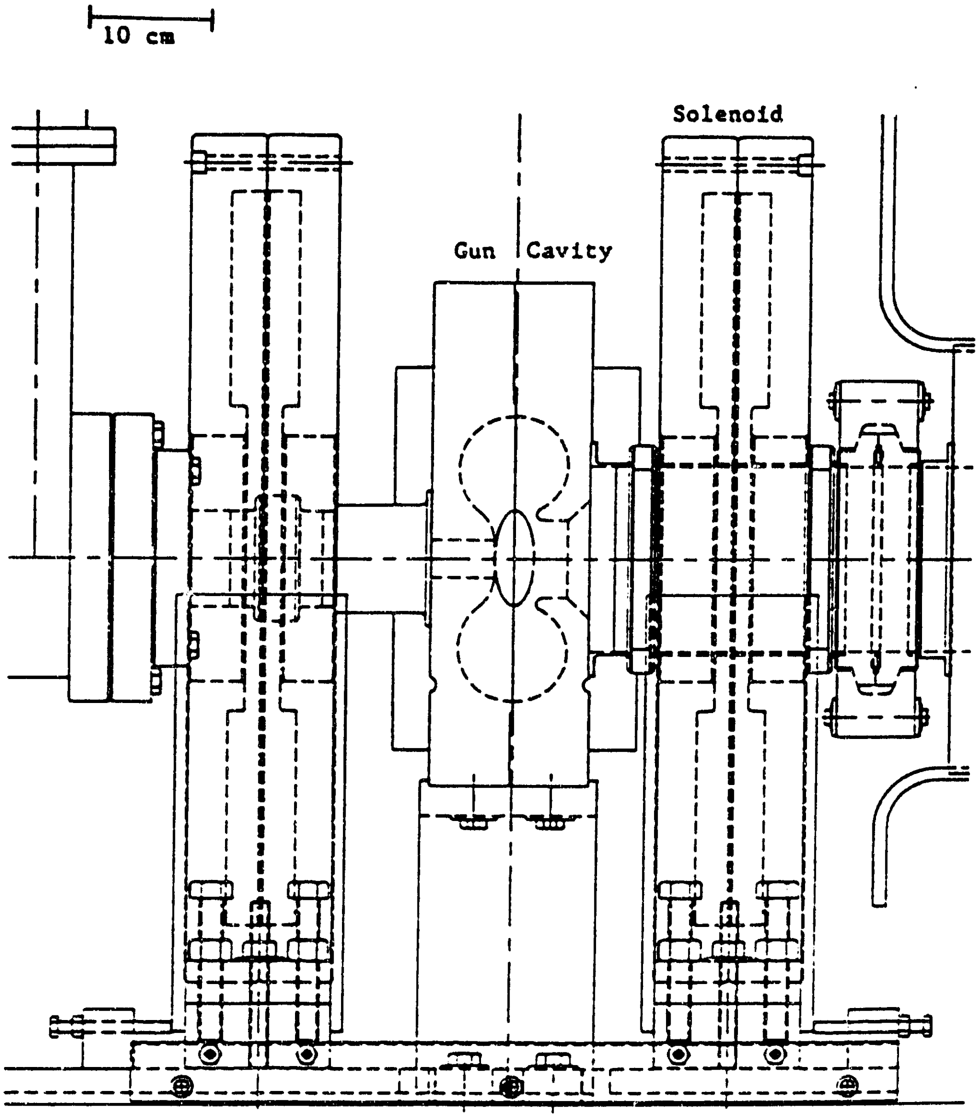

Figure 2.1.4: Engineering drawing of the photocathode rf gun cavity and solenoids. This shows the R-Z cross section for an axially symmetric system. The radial direction (R) is drawn vertically and the axial direction (Z) is drawn horizontally. The electron beam travels from left to right.

After phase-I of the AWA, additional drive acceleration consisting of several travelling wave linac tanks similar to the preaccelerator will be built to increase the drive beam energy to around 150 MeV. Since the increased beam rigidity in the drive linac implies less sensitivity of the beam to transverse wakefields, a smaller iris size than that of preaccelerator may be used to increase the shunt impedance and consequently the power efficiency.

For a collinear wakefield accelerator in which the driving beam and the witness beam traverse the wakefield device through the same straight line path, there is a fundamental theorem of beam loading, called the Wakefield Theorem, which puts a limitation on the energy gain of the witness beam.[6] This theorem states that the transformer ratio, which is the ratio of the maximum energy gained by a particle in the witness beam to the maximum energy lost by a particle in the driving beam, is limited to be less than two in a collinear wakefield device. That means while a more intense driving bunch produces a higher accelerating gradient for the trailing bunch, the acceleration can be maintained for a shorter distance. This problem complicates practical applications of wakefield accelerators.

One method to improve the transformer ratio is the wakefield step-up transformer.[26,29] Figure 2.1.5 illustrates the principle of this scheme. The rf power is generated in a large-diameter wakefield tube (stage I), where deflection mode generation by the intense drive beam is tolerable. The rf power is then fed into a small-diameter acceleration tube (stage II) through a quarter wave transformer, where the less intense witness beam is accelerated by the greatly enhanced axial electric field. The witness beam generates little deflection-mode power itself, even in the small acceleration tube. Thus a final high quality, high energy electron beam is produced.

A multi-stage wakefield acceleration scheme was also proposed to overcome the limitation of the transformer ratio.[27,30] The idea is to use a train of several driving bunches and a sequence of wakefield devices to accelerate one witness beam. The AWA will produce one witness bunch and a train of 4-5 drive bunches by optical splitting of the laser pulse. The energy differences between bunches due to the beam loading and variation of acceleration phase for individual bunches will be utilized to magnetically separate them after exiting the drive linac. Each drive beam will then enter a wakefield device preceding the witness beam in a subsequent order. After most of the driving beam energy has been transferred to the witness beam in one wakefield device, the dissipated driving bunch is then discarded and the witness beam enters the next wakefield device behind another fresh driving bunch at full energy to continue the wakefield acceleration process until the designed goal of 1 GeV is met.

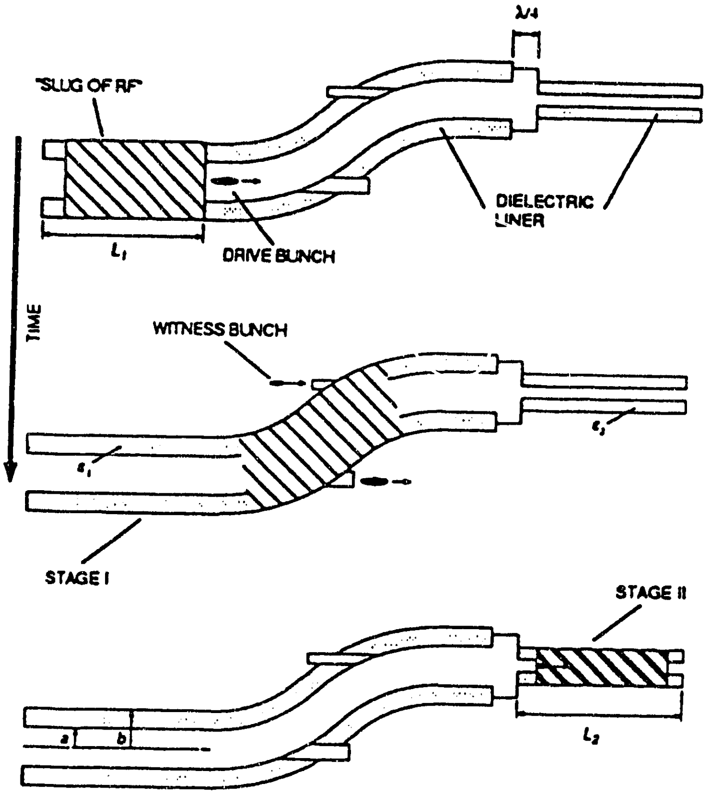

Figure 2.1.5: The wakefield step-up transformer using dielectric-lined waveguide with a hollow waveguide quarter wave matching section.

2.2 DESIGN PRINCIPLES

Now, let's concentrate on the components for the phase-I of AWA. As mentioned before, the goal for phase-I is to generate the electron drive bunches with the charge and bunch length being on the order of 100 nC and 10 ps respectively. The huge space charge force for such a high current, short pulse beam is the main concern of the design. The development of photocathode based electron source technology over the past few years[31,32] is extremely useful for short electron bunch generation. The underlying principle for these sources is to place a photocathode in the end wall of an rf cavity. A well processed rf cavity can support very high electric fields on the order of 100 MV/m on the cathode surface. At some phase of the field, a short laser pulse impinges on the cathode which in turn emits a short burst of photoelectrons. Large initial space charge self forces are quickly reduced by the rapid gain in the energy of the ejected electrons under the acceleration of very strong electric field.

The laser photocathode also offers some advantages over the thermionic cathode: (1) The energy spread of the laser photo-emitted electrons is relatively small. (2) The total charge produced is proportional to the incident laser power. (3) There is no intrinsic limit on the emittance and current density. (4) The electron beam can be easily shaped by adjusting the laser beam optics. We can take advantage of (4) to reduce initial space charge forces.[33,34] If the incoming laser beam is tailored to have a concave wavefront, then the emitted photoelectrons form a curved bunch. The effect of the curved beam is to considerably reduce the instantaneous charge density and hence the space charge forces near the photocathode, at the expense of an initially longer bunch length. The electrons are produced with a strong positive correlation between angular divergence and initial radial position, and also between radial position and time. If allowed to drift, the electron at larger radii tend to axially lag those at small radii. Thus, the bunch length is effectively compressed at later time. Figure 2.2.1 illustrates this idea from an example of simulation results for the temporal evolution of a single bunch. We will discuss beam dynamics simulations in the next chapter.

A solenoid downstream of the rf gun cavity is used to control the transverse size of the bunch and permits matching to the aperture of the preaccelerator. We are going to describe each component further in the following sections.

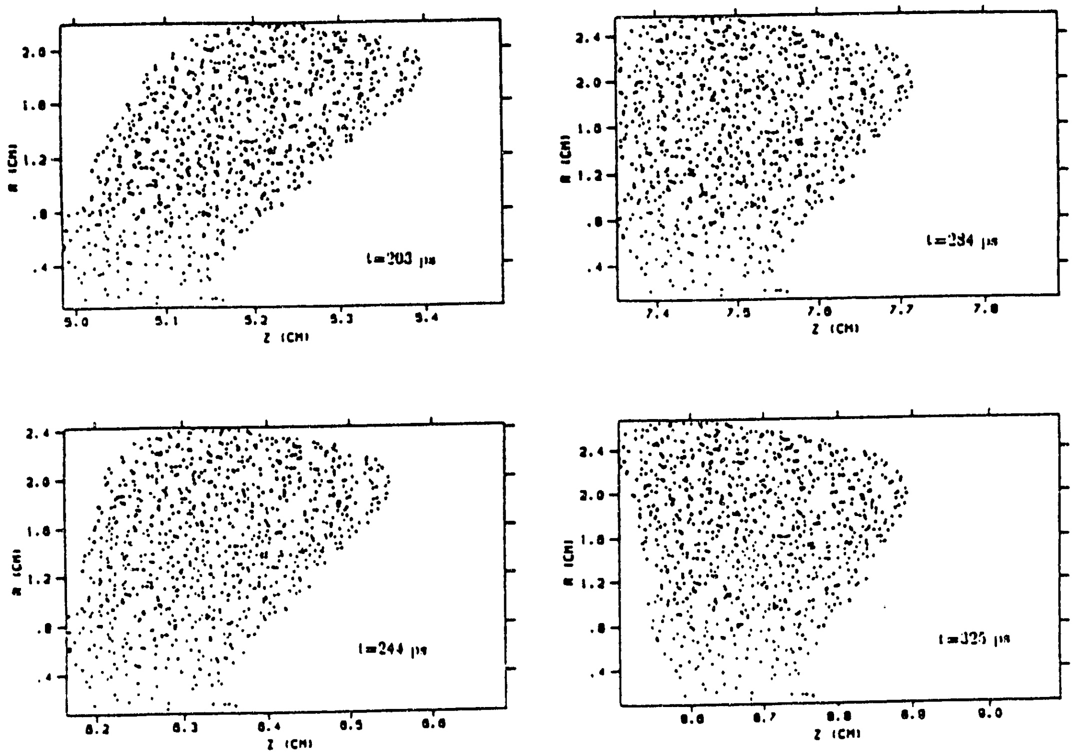

Figure 2.2.1: Temporal evolution in real space of a drive beam showing the flattening of the curved bunch after the gun exit. R is the radius and Z is the distance from the cathode surface.

2.3 PHOTOCATHODE RF CAVITY

The design of the photocathode based electron source draws heavily upon recent developments at LANL and BNL. While their efforts are directed toward extremely bright, high repetition rate devices, our needs are significantly different. The maximum tolerable emittance for our source is much larger so that even with our much larger charge within a bunch, our source brightness is an order of magnitude smaller than those of LANL and BNL guns. The desired repetition rate is also much lower (30 Hz). Our parameters have the effect of greatly relaxing many of the demands on the source components.

The role of the rf gun cavity is to accelerate the electrons from the photocathode to relativistic energies sufficiently rapidly that longitudinal and transverse space charge blowup of the beam is minimized. The problem of cavity design is one of maximizing the accelerating gradient at the photocathode, subject to the constraints of operating frequency, available drive power, stored energy, and peak surface fields.

Our cavity design is shown in Fig. 2.3.1, with the electric field vectors for the fundamental mode superposed. The cross sectional shape was chosen to be nearly circular to maximize stored energy. This is graded smoothly to a flat photocathode region and to a nosecone which serves to concentrate the fields at the photocathode. A large photocathode area with 2 cm diameter was used to reduce space charge forces and the laser power density on the cathode surface. The possibility of using a curved photocathode surface was also briefly considered, but was ultimately rejected as being less flexible than the curved wavefront scheme. The fields and other cavity parameters are calculated using the code URMEL. URMEL[35,36] is an eigenmode finder. It computes resonant modes in cavities and frequencies of longitudinally homogeneous fields in waveguides for cylindrically symmetric accelerating structure. The cavity geometry was iteratively adjusted to obtain the desired frequency and accelerating gradient. The design was also checked against the SUPERFISH code. SUPERFISH[37,38] also evaluates the eigenfrequencies and fields for arbitrary-shaped 2D waveguides in cartesian coordinates and 3D axially symmetric cavities in cylindrical coordinates. Assuming 1.5 MW input power, Fig. 2.3.2 plots the amplitude of the longitudinal electric field E_z along the axis of the gun cavity and Table 2.3.1 lists some of the operating parameters.

Table 2.3.1: Gun cavity parameters.

Frequency (GHz)	1.30
Length (cm)	5.75
Inner Radius (cm)	7.52
Aperture (cm)	1.99
Quality Factor, Q	15000
Input rf Power (MW)	1.5
Stored Energy (Joule)	2.8
E_z at Cathode (MV/m)	92
Peak Surface Electric Field (MV/m)	127

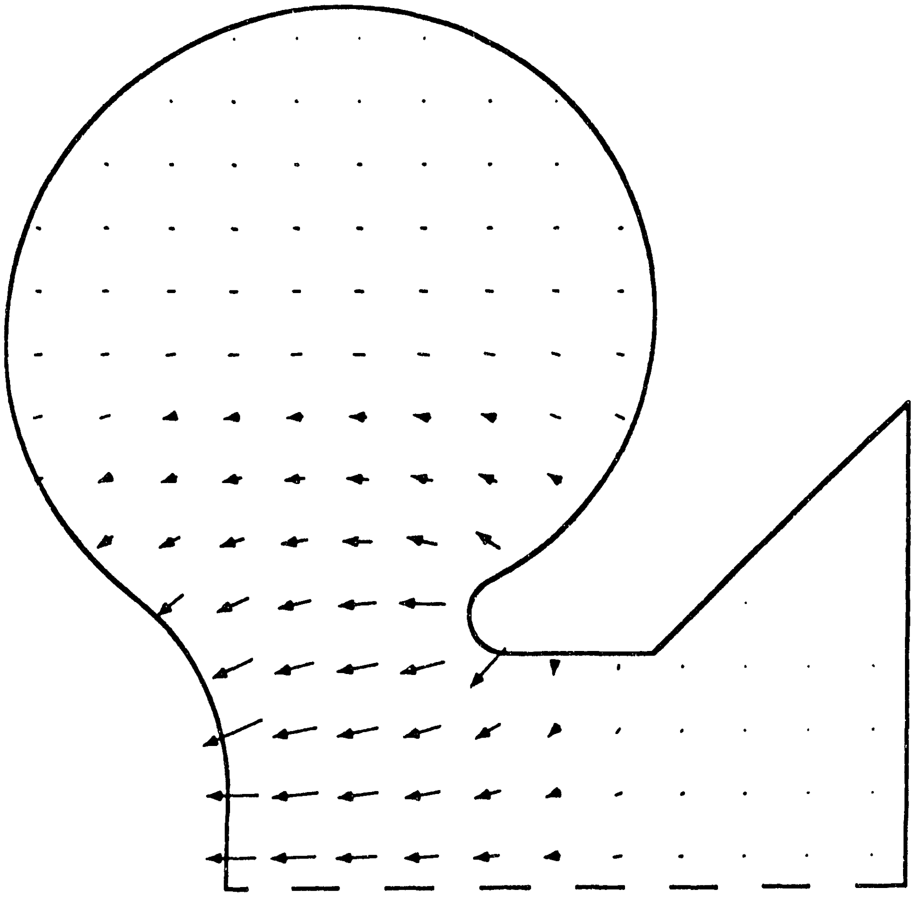

Figure 2.3.1: R-Z plot of the AWA gun cavity and electric field vectors. The radial direction (R) is drawn vertically and the axial direction (Z) is drawn horizontally. The electron beam travels from left to right.

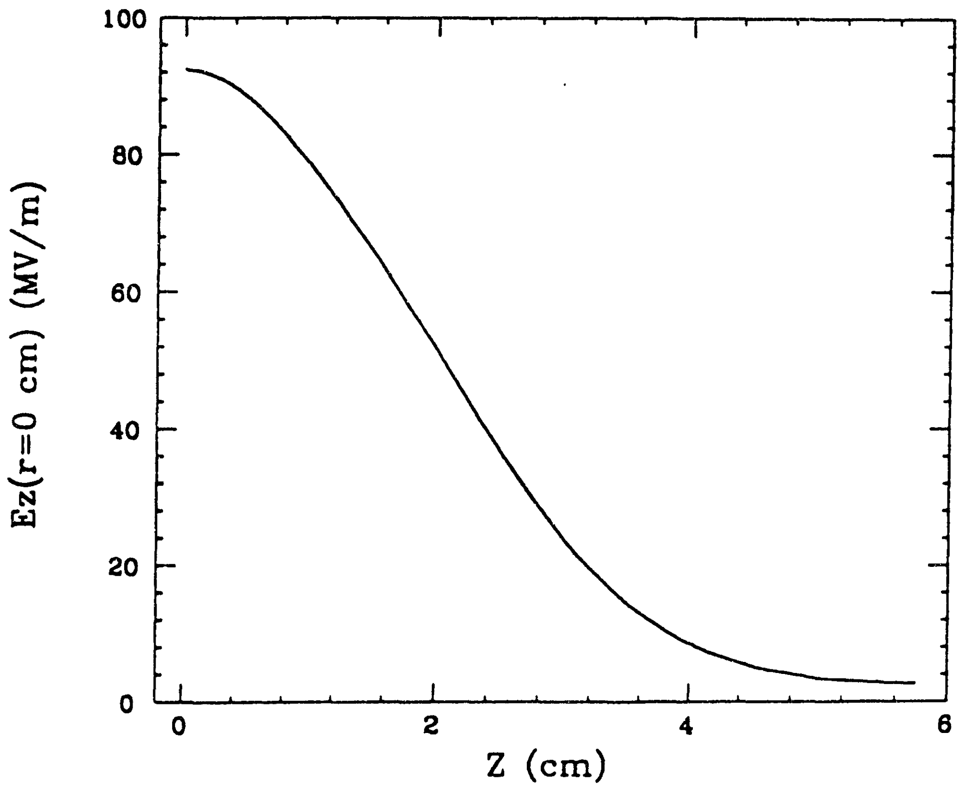

Figure 2.3.2: Longitudinal electric field distribution along the gun cavity axis. Z is the distance from the photocathode surface.

2.4 LASER SYSTEM

An advanced laser system is an essential element of the AWA source. As described previously, a laser photocathode cavity will be employed to produce short intense electron pulses. Based on experimental results of the Brookhaven National Laboratory,[39] for a photon energy of 4.66 eV (266 nm), the quantum efficiency (electrons emitted per incident photon) is 5.0×10^{-4} for Yttrium and 7.5×10^{-4} for Samarium. For the current design, we have chosen Yttrium as our photocathode material for its less stringent vacuum requirements. In order to generate a 100 nC electron pulse, a laser capable of producing at least 1 mJ per pulse is required. This laser system was found commercially available and was purchased last year (1991). Installation started on November 1991, and completed April 17, 1992. A block diagram of the laser system is shown in Fig. 2.4.1. Table 2.4.1 shows the laser parameters of the AWA laser system.

Table 2.4.1: AWA laser parameters.

Operation Wavelength (nm)	248
Laser Pulse Length (ps)	≤ 3
Energy per Pulse (mJ)	8 - 15
Repetition Rate (Hz)	30
Timing Jitter (ps)	≤ 5
Amplitude Jitter (peak to peak)	$\leq 13\%$

The concave laser wavefront described before can be generated using a device shown in Fig. 2.4.2. Ten concentric cold-rolled steel pipes will be mounted friction tight against each other, looking like telescoping tubes. One end of each tube is connected with its neighbor to a stepper motor. Each motor will control the relative motion between one tube and all other tubes outside of it. The other end of each pipe will be polished and coated as a mirror surface to reflect the incoming laser light. Since the mirror surface positions can be moved by the stepper motors to form a concave shape, the laser wavefront will be shaped accordingly. The motion of the stepper motor will be remotely controlled by the computer.

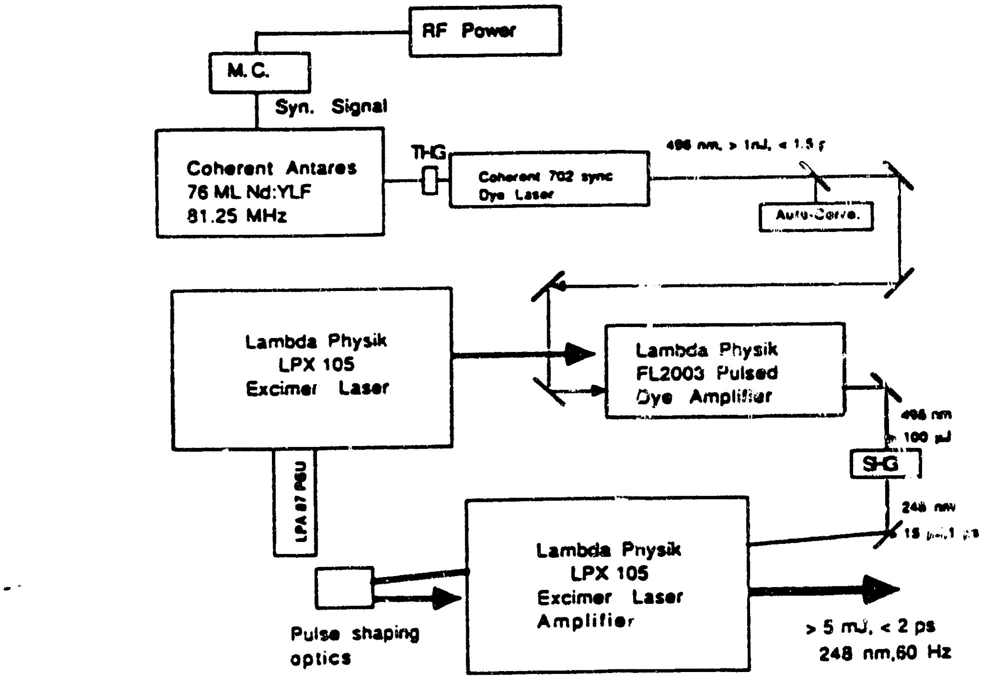

Figure 2.4.1: Joint Coherent Lambda laser system for AWA rf photocathode.

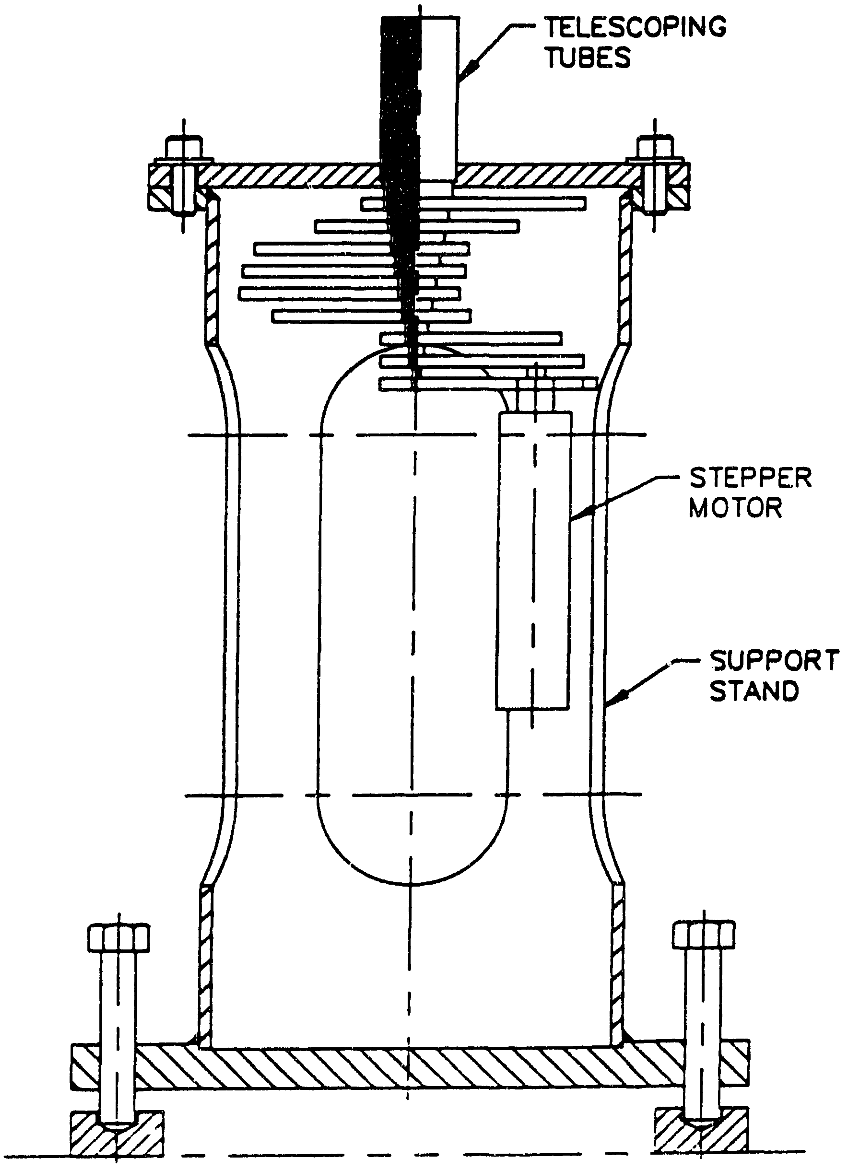

Figure 2.4.2: Laser pulse shaping reflector.

2.5 PREACCELERATOR CAVITY

The purpose of the preaccelerator is to boost the drive bunch with a charge of 100 nC from the injection energy of 1.5-2 MeV to an energy of 20 MeV.

Examining the constraints on the system, we realized that these design goals differ from many existing linacs only in the magnitude of the beam currents involved. Wakefields, which will be used constructively elsewhere in the facility, are a potential source of problems in the preaccelerator and drive linac, and suggest deviations from typical linac designs. Indeed, the preaccelerator is of the standing wave type, rather than the more efficient traveling wave type, to minimize the effects of parasitic wakefields in the structure. Design of the preaccelerator proceeded iteratively, optimizing the accelerating properties (Q, shunt impedance, group velocity) computed by URMEL, while using TBCI[40,41] to minimize transverse wakes.

The preaccelerator cavity design is an iris-loaded standing wave structure operating in a $\pi/2$ mode. Loew and Neil[42] discuss the relative merits of various modes, and determine that in order to minimize beam loading effects and sensitivity to dimensional errors $\pi/2$ mode is an optimum choice. The cavity will consist of 36 cells, each 5.756 cm in length, resulting in a total length of 2.07 meters. Each cell will be 10.0 cm in radius, and each iris will be 5.08 cm in radius, with a length of 0.5 cm. Note that to reduce wakefield effects, an iris radius of 5.08 cm, which is much larger than that in traditional L-band linacs, is used. As a result of this big iris aperture, we have a large group velocity of 0.17 c.

Therefore the preaccelerator is operated in the standing wave mode to achieve an average acceleration gradient of around 8 MeV/m with an input rf power of 10 MW/m. Four cells of the preaccelerator with the electric field vectors superposed as computed from URMEL is shown in Fig. 2.5.1.

We split the preaccelerator into two sections because it's easier for support and shipping, less likely damaged and also leaves room for the second solenoid.

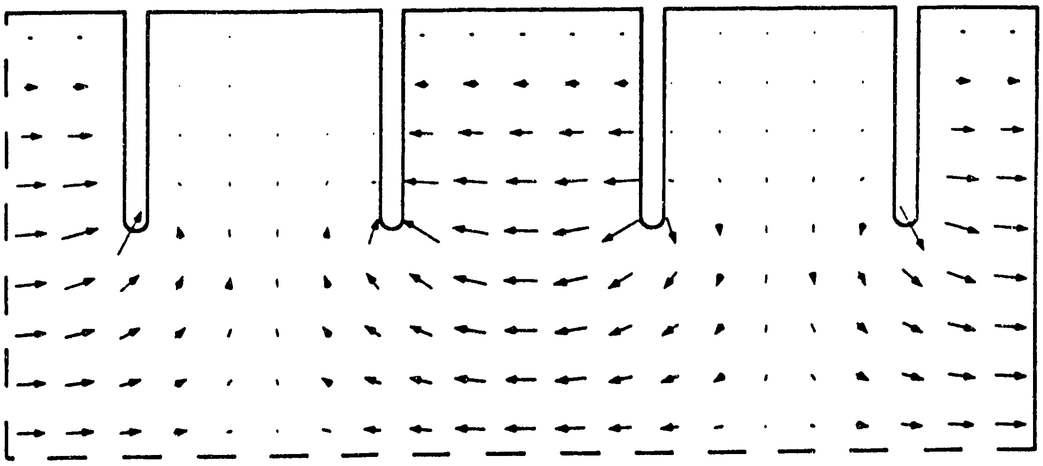

Figure 2.5.1: R-Z plot of a four-cell preaccelerator cavity and electric field vectors. The radial direction (R) is drawn vertically and the axial direction (Z) is drawn horizontally.

2.6 SOLENOIDS

Below about 15 MeV, the primary beam optics problem is to control the very large divergence produced at the photocathode and to focus the beam through the preaccelerator section. Wakefield considerations require that while the beam position must be closely controlled, the beam size is not critical, and in fact should be large at low energies to minimize space charge effects. Focusing in the photocathode gun and the preaccelerator is accomplished with solenoids.

As we see from Fig. 2.6.1, an interesting feature of the drive beam after exit of the gun cavity is that there's a correlation between the energy and radius of the electrons. At a larger radius, electrons have bigger momentum. Since the focal length increases as the square of the beam momentum but decreases as the square of the solenoid field, we would like to have bigger field strengths at larger radii so that all electrons can be focused to about the same waist. Therefore, our solenoids are preferred to possess some degree of spherical aberration. It was also found the spherical aberration is sensitive to pole geometry of the iron core.[43] A real solenoid with coils and the iron core was designed using the code PE2D. PE2D[44] is a finite element POISSON solver. It is a 2D code for the analysis of electrostaic or magnetostatic fields, and steady state and transient eddy currents. PE2D enables the solution of the partial differential equation governing a system to be computed using the finite element method. The present design used in the beam dynamics simulation has a bore radius of 6.5 cm, a pole width of 1 cm, and a gap distance of 1.778 cm. It takes 10000 amp-turn to produce a peak B-field of 1480 Gauss on the axis.

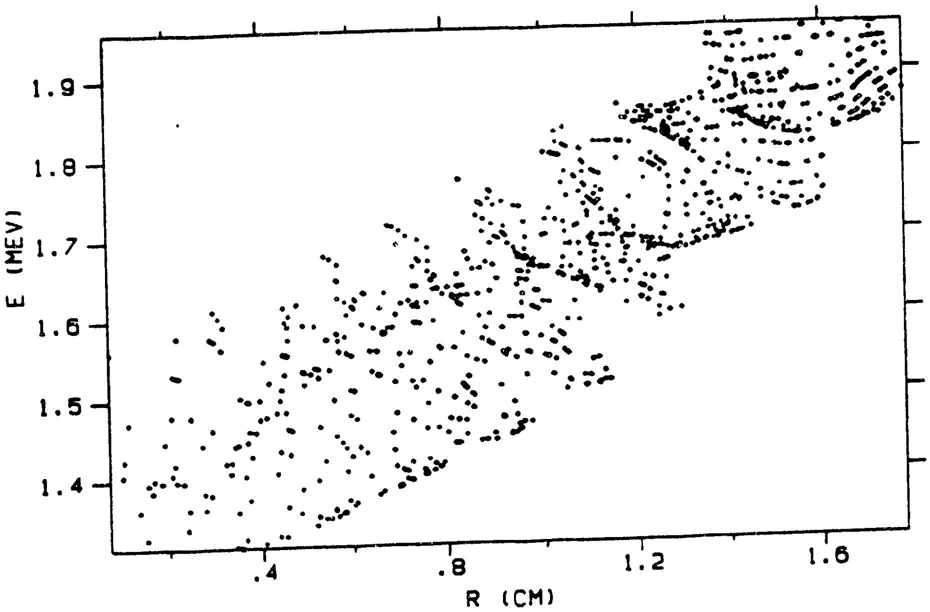

Figure 2.6.1: Energy versus radius of electrons at gun exit.

2.7 WITNESS GUN

In the original design for the AWA, we had planned to use a single photocathode gun for generation of both the drive beam and the witness beam. In this scheme two separate laser pulses would strike the photocathode. The laser pulse generating the witness beam is phased to provide the witness beam energy at 10 MeV. The time delay between the two beams was to be controlled by a trombone section similar to the one used in the AATF. A major drawback to this scheme was found by the PARMELA simulation of the witness beam. For optimized drive beam parameters, the witness bunch emerged from the preaccelerator with a very large divergence, making the optics design of the trombone section nearly intractable.

In the current design plan for the AWA, we have decided to use a separate rf photocathode gun to generate the witness beam thus enabling the witness parameters to be controlled independently. We are currently looking into the possibility of using a dielectric loaded rf cavity for the acceleration of the witness beam. It is believed that this dielectric loaded cavity will be able to generate a high brightness beam. Historically, dielectric loaded cavities used to accelerate beams have been frowned upon by the accelerator community. This method presents two obstacles, the charging of the dielectric and the fact that dielectrics are lossy. If the dielectric is too lossy, an unreasonable amount of power will be required to achieve a meaningful accelerating gradient. If the dielectric is a very low loss material, then the charging of the dielectric may occur. We have decided to use an extremely low loss material, alumina. This has a loss tangent of 0.0001.

We plan on confining the beam to the center of the cavity so as to keep charging from becoming a problem. If this method is not feasible, a conventional copper rf accelerating cavity will be used for generation of the witness beam.

Since the two beams originate from different locations, we are now faced with the problem of making the witness beam collinear with the drive beam. The solution arrived at is shown in Fig. 2.7.1. Both drive line and witness line are achromatic. The two beams enter into a circular pole magnet and emerge from it collinear. The witness beam is bent through an angle of 25° while the drive beam is bent through an angle of 5°. This 5:1 ratio in bending is due to 5:1 ratio in beam energies. If the ratio of the beam energies comes out different from 5:1, as it likely will, we must be able to tune the line. Once we know the energy of the witness beam, its direction into the circular pole magnet will be fixed. The direction of the drive beam will be adjusted until it emerges collinear. This ability to adjust the drive beam's direction can be achieved as follows. The first two bending magnets of the drive beam triplet can be varied in strength, while the position of the center magnet of the triplet is simultaneously changed in such a way as to allow the beam to emerge collinear.

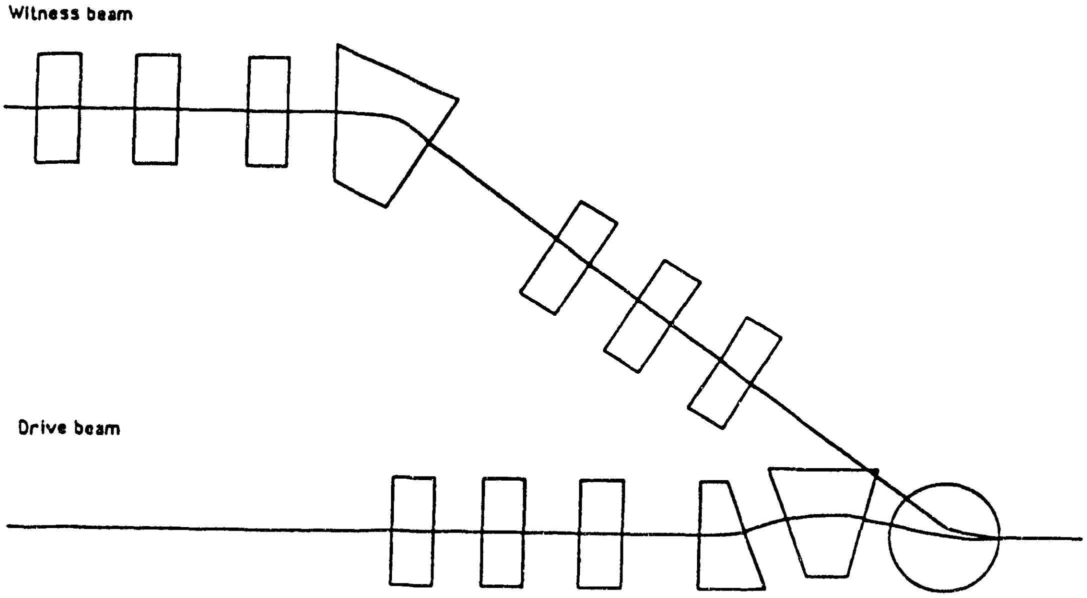

Figure 2.7.1: Schematic of the beam optics to make the witness beam collinear with the drive beam before entering the wakefield device. Both beams travel from left to right.

2.8 VACUUM SYSTEM

Vacuum level requirements vary over the length of the accelerator, from 1×10^{-6} torr in the drive linac and wakefield sections, to 1×10^{-9} torr in the photocathode gun. (Note that the vacuum requirements for a Yttrium photocathode are less stringent than for high quantum efficiency materials.) The high vacuum in the gun cavity will be developed using an ion pump/turbomolecular pump/roughing pump combination, and will be monitored and controlled by a standard Bayard-Alpert ion gauge tube controller. The less severe vacua allowable further down the accelerator will be developed using turbomolecular/roughing pumps monitored by Bayard-Alpert/thermocouple vacuum gauge controllers. Diagnostic boxes placed between accelerator sections will each have a vacuum coupling port to allow for connection of a vacuum pumping unit. Three turbomolecular/roughing pump assemblies will be used to maintain $< 1 \times 10^{-6}$ torr pressures in the accelerator. Extra ports will be provided to allow for additional pumping if necessary.

2.9 DIAGNOSTICS

The electron beam diagnostic techniques are for the most part extensions of those which have yielded good results in the AATF. Transverse beam position monitors consist of luminescent screens inserted into the beamlines by means of pneumatic actuators. SLC-type anodized aluminum screens are a good candidate based on robustness and vacuum criteria. Light from the phosphors is detected by CCTV cameras. The camera signals are fed to a multiplexer, which then allows computer selection of the desired diagnostic channel. A VME based video digitizer is used to acquire frames for analysis or storage on disk. A VCR will be available for real time image recording.

At least for the lower energy stages, the luminescent screens could be backed with an absorber to act as Faraday cups. At higher energies, where the beam is no longer completely stopped in the absorber, Faraday cups are still potentially interesting as relative intensity monitors. It is also useful to have the capability of inserting emittance plates for measuring and optimizing the transverse emittance as part of the normal linac tuneup. Additional nondestructive diagnostics such as Rogowsky coils may be included as a performance monitor during routine linac operation.

Pulse length diagnostics consist of Cherenkov cells with an optical transport system to bring the light to a streak camera. A significant change from the AATF is the integration of the streak camera controls with the main data acquisition system, instead of relying upon the streak camera manufacturer's controls and software.

2.10 CONTROL SYSTEM

The design of the AWA control system is based in part on experience gained at the Advanced Accelerator Test Facility, and also on more extensive data acquisition systems used for high energy physics experiments. The goal of the AWA control system is to provide easy selection and adjustment of accelerator and beamline parameters, as well as the online analysis of diagnostic and physics data. Other necessary functions are the storage and recall of working parameter sets and the automatic monitoring of component performance (and flagging of deviations from preselected tolerances).

A RISC based workstation, the HP-Apollo 750, using the UNIX operating system was found to supply the most cost effective solution, and at the same time maintain broad vendor independence and compatibility with the accelerator physics and engineering software base.

A block diagram for the AWA computer control system is shown in Fig. 2.10.1. The workstation is interfaced to a VMEbus based control system. In addition to the routine operation of the accelerator (rf power supply control and monitoring, beamline tuning, drift monitoring and compensation), the computer will be used to analyze video images from the beam position monitors and streak camera system. The requirement of carrying out rapid image feature extraction from large quantities of data requires high floating point performance.

Initially most of the control and monitoring functions will be handled through a VME-CAMAC parallel bus interface. Video signals from beam position monitors and from the streak camera, comprising the actual physics data from the experiment, are acquired using a high resolution VME-based frame grabber with 512 by 512 pixels and 256 level gray scale.

Experience with the AATF control system has demonstrated the importance of rapid online data analysis for wakefield measurements. This procedure (on a frame by frame basis) consists of fitting edge data to a model of the background, performing a background subtraction, and extracting moments of the resulting 2D beam intensity distribution. In order to be able to accomplish this in near real time, it is essential that the control computer be capable of high floating point performance.

The color graphics terminal will be used as an integral part of the control and data acquisition system, permitting data to be displayed online, both in the form of plots and processed/enhanced video images. The menu-driven control program will require real time interaction between the linac operator and the graphical interface. Offline programs will utilize the graphics display for visualization of data.

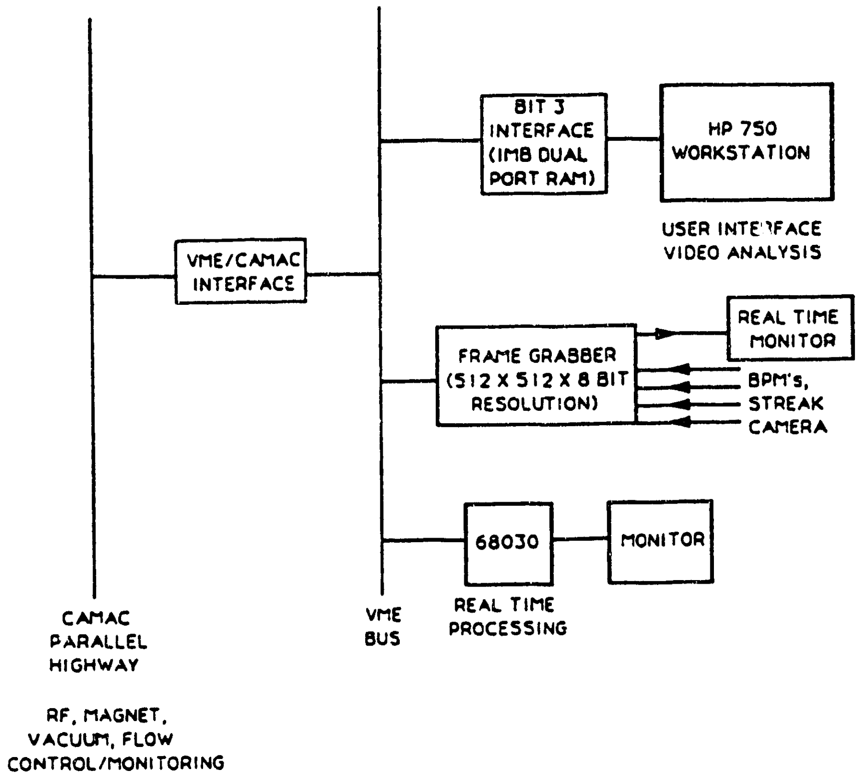

Figure 2.10.1: Block diagram of the AWA control system.

3 Beam Dynamics Simulations

The particle-in-cell codes, TBCI-SF and PARMELA, which were used in beam dynamics simulations for the gun and the preaccelerator are described. Several modifications made to PARMELA for proper treatment of the high current, short bunch beam are presented. We also made an estimation of the space charge force and compare results to those of simulations from modified PARMELA. The simulation procedure to get optimum parameters for the AWA operation is then explained and optimized results are illustrated. The effects of sagitta, laser amplitude jitter and timing jitter around the operating regime are also discussed.

3.1 SIMULATION TOOLS

Two particle-in-cell simulation codes were used to study the beam dynamics for the Phase-I of the AWA. They are PARMELA[45] and TBCI-SF.[46] Both codes assume a three dimensional cylindrical geometry. While TBCI-SF is a full electromagnetic particle simulation code, PARMELA calculates the space charge forces in a reference frame which is co-moving with the beam and then uses Lorentz transformation to come back to the laboratory frame. TBCI-SF also analyzes the electromagnetic interaction between bunched beams of charged particles moving through cylindrically symmetric cavities by calculating wakefields.

We used TBCI-SF for simulation of the beam dynamics in the rf gun cavity and then save the phase space data for conversion into a form readable by PARMELA. PARMELA was then used to track the particles through the preaccelerator. The reason we did not use TBCI-SF for the preaccelerator is due to the memory size restriction because the preaccelerator is much longer than the gun cavity. While TBCI-SF uses a fixed mesh to cover the whole preaccelerator, PARMELA adopts a moving grid to cover the entire beam and thus avoids the memory size problem. The problem without using PARMELA for the gun cavity is that PARMELA does not include wakefield effects. From estimations[26] made using TBCI, the effect of the longitudinal wakefield in the preaccelerator is only to increase the energy spread by about 10%, while it is about 30% to 40% increase for the gun cavity. Therefore we can not ignore the wakefield effect in the gun cavity since the energy spread will cause serious chromatic effects when the beam is focused by the first solenoid downstream of the gun.

The cavity fields were calculated from the code URMEL and the solenoid magnetic fields were designed by the code PE2D. These fields were then converted to a format readable by PARMELA. URMEL gun cavity fields were also used in TBCI-SF.

3.2 PARMELA AND OUR MODIFICATIONS

In this section, we are going to describe in detail our modifications to the simulation code PARMELA.

As advertised, PARMELA is a versatile multi-particle code in which the electron beam, represented by a collection of particles, may be transported through a linac or other transport system specified by the user. The name, PARMELA, is derived from the phrase, "Phase and Radial Motion in Electron Linacs".

The first step to adapt PARMELA in simulating our 100 nC , concave shaped beam is to replace the subroutine INPUT with a subroutine which allows electrons to be emitted from the photocathode only within the region covered by the shaped laser beam at a specific time step. Thus the electrons will first be emitted from outer rings of the photocathode and subsequently from inner rings as the area of the cathode where the laser beam illuminates converges inward to the axis. This was termed 'dynamical' emission of electrons in Ref. 34, in contrast with the initial static distribution of electrons in the unmodified subroutine INPUT of PARMELA. The dynamical emission of electrons is certainly much closer to the real physical situation. There are three options for beam shaping at present: one for flat beam shape, one for concave beam shape, and the last for the arbitrary beam shape. The added input subroutines are called from the subroutine PARDYN, which controls the logic of particle dynamics calculations, instead of being called before dynamics calculations. For convenience, the INPUT card is retained but now has the following parameters: vv(1)=radius of curvature of cathode (cm, use 0 for flat cathode), vv(2)=radius of cathode (cm), vv(3)=sagitta of the concave laser wavefront (cm), vv(4)=pulse width of the laser beam (ps), vv(5)=initial angular spread of transverse momentum (mR), vv(6)=flag for beam shape (0 for flat shape, 1 for concave shape, else for arbitrary shape), vv(7)=total number of time steps during emission of particles from cathode, vv(8)=average number of particles emitted per time step, vv(9)=total number of particles emitted (not including the reference particle).

The subroutine SCHEFF calculates space charge forces among particles and deserves special attention since space charge effects play an extremely important role in beam dynamics for our high charge (100 nC), short pulse (10 ps) electron beam generation. It was found that space charge forces are dependent on the space charge grid if the grid size is much larger than the distance between simulated particles, especially in the early acceleration stage during the dynamical emission of electrons. If we use a very small mesh size in the beginning to be compatible with the beam size, which is of the order of one hundred microns during dynamical emission, then most of the particles will go outside the mesh when beam size grows later. The easiest way to solve this problem is to use the actual beam size, which is varying in time, as ZMESH and RMESH (longitudinal and radial mesh size, respectively) instead of using the fixed input values of ZMESH and RMESH from the SCHEFF card. Since the mesh size is changing with time, the field table has to be re-calculated every time SCHEFF is called and this increases computation time. Therefore it would be nice to come back to the 'fixed' mesh size method when the beam energy begins to approach the relativistic limit. The RESTART card, which will be described later, can be used for this purpose. The other modification made in subroutine SCHEFF is to write out the total number of particles outside the space charge mesh which will not be included in the space charge force calculations instead of just giving a single warning for the first outside mesh particle. The parameter maxdim in SCHEFF also increases from 8000 to 65535 (upper limit in VAX 3800 machine). This enables us to increase NZ and NR (number of longitudinal and radial mesh intervals, respectively) so that it is possible to reach a finer grid size (=ZMESH/NZ, longitudinally, and RMESH/NR or RMESH*RMESH/NR depending on OPT, radially). In figure 3.2.1, the longitudinal width of the beam at a specific radial position (R=0.8 cm) and a specific time (T=81.25 ps, nt=500 time steps) is plotted as a function of NZ (number of longitudinal mesh intervals) using the dynamical longitudinal mesh size method with fixed RMESH=3.6 cm and NR=54. From Fig. 3.2.1, the longitudinal width of the beam, which is affected by space charge forces, finally reaches a plateau region after increasing NZ to be greater than 10 (i.e., much finer grid size=ZMESH/NZ). This means the space charge forces are independent of the space charge grids if we use the dynamical mesh size method and make NZ large enough to be in the plateau region. From this fact and the estimations on the space charge forces in the next section, we are confident that our modifications to PARMELA are physically reasonable.

As advertised in PARMELA, the RESTART card provides the means of changing the beam line from run to run and restarting the calculation just before the part that has changed without running the entire problem from the beginning. It can save a lot of time. And as mentioned earlier, RESTART can also serve as an alternative way to vary RMESH and ZMESH from time to time to obtain the smallest mesh size which covers the entire beam after we come back to the 'fixed' mesh size method. Unfortunately, this did not work because the original PARMELA saves only the data of CORD, WT, and NGOOD, which are not sufficient to restart properly. In addition to the above data, we now also save the following: NPOINTS, MT, NEL, LTYPE, FREQ, WAVEL, IPNUM, NE, NBUF, NEB, GAM, ZLOC, W0, IXX (random number seed). Furthermore, the original PARMELA assumes pure DRIFT (without any field) after particles pass the end of last element which is not correct if the first element after restart is not DRIFT. Therefore, to utilize RESTART without a drift space at the beginning of the subsequent element, the initial run is performed up to the next to the last element which is specified as the first element in the subsequent run. We double checked this modification by comparing the data of CORD between a restart run and a straight run. We are now able to restart a PARMELA run from any time step.

Another modification regards the processing of several PARMELA runs in parallel in the same working disk area. This may be desired for, say, quick comparison of several configurations. This is accomplished by opening the data files of savecor and ntape, etc., at appropriate times so that there will be no confusion among different versions of data files.

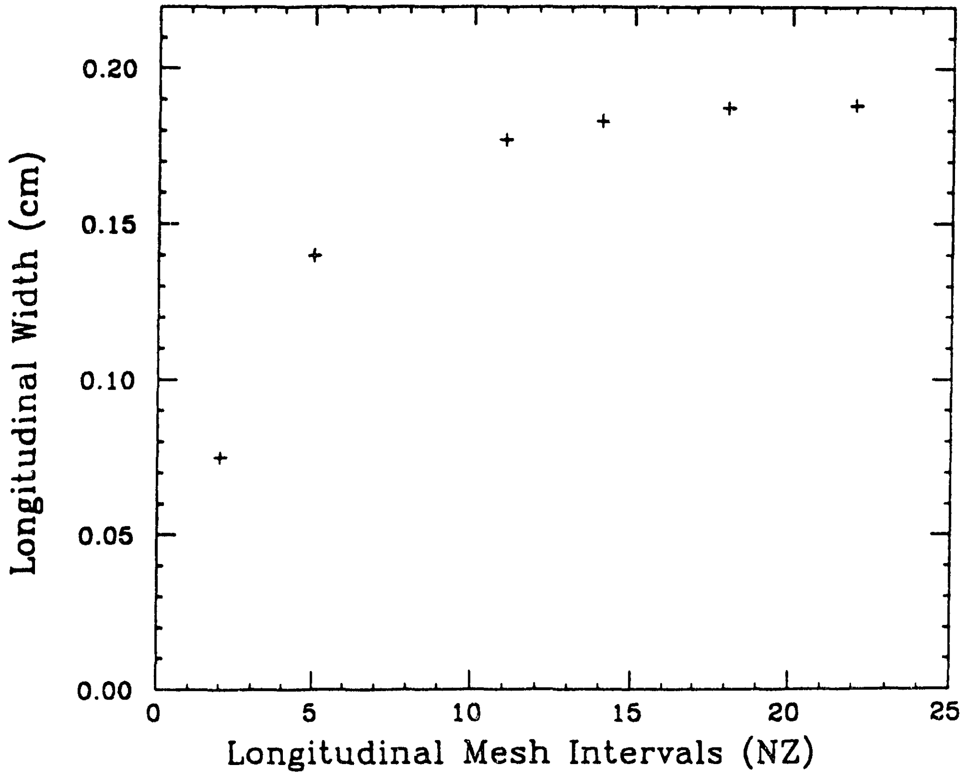

Figure 3.2.1: Insensitivity of space charge forces to mesh size in PARMELA simulation. The longitudinal width of the beam, which is affected by space charge forces, reaches a plateau region when the number of mesh intervals (which is inversely proportional to mesh size) is greater than ten.

3.3 ESTIMATION OF THE SPACE CHARGE FORCES

An exact analytical treatment for the space charge forces is almost impossible for the many particle system. That's why beam simulation plays an important role in the study of beam dynamics. However, we can make an estimation of the space charge forces under a reasonable assumption and compare the calculation results to those of simulations from PARMELA.

The simple assumption we are going to make is that all the electrons in the bunch are moving with the same velocity, $v(=\beta/c)$, in the z-direction. This assumption is feasible in simulation since we can let the beam drift at any constant velocity. It is easier to work in the reference frame moving with electrons since the electromagnetic interaction is completely described by a purely electrostatic field $\mathbf{E}'$. The longitudinal and transverse electric field components , E_z and E_r respectively, in the laboratory frame are given by the Lorentz transformation

$$E_z = E'_z \text{ and } E_r = \gamma E'_r \quad , \tag{1}$$

where $(\gamma - 1)mc^2$ is the kinetic energy of the electrons.

For a cylindrically symmetric charge distribution, the general solutions of E'_z and E'_r at an observation point (r_0, θ_0, z_0) for a concave shape beam as shown in Fig. 3.3.1 are

$$E'_z(r_0, \theta_0, z_0) = \frac{\rho}{4\pi\epsilon_0} \int_0^{r_0} r dr \int_0^{2\pi} d\theta \int_{z_1(r)}^{z_2(r)} \frac{(z - z_0)dz}{d^{3/2}} \tag{2}$$

$$E'_r(r_0, \theta_0, z_0) = \frac{\rho}{4\pi\epsilon_0} \int_0^{r_0} r dr \int_0^{2\pi} d\theta \int_{z_1(r)}^{z_2(r)} \frac{(r_0 \sin\theta_0 - r \sin\theta)dz}{d^{3/2}} \quad , \tag{3}$$

where

$$
\begin{aligned}
d &= (r\cos\theta - r_0\cos\theta_0)^2 + (r\sin\theta - r_0\sin\theta_0)^2 + (z - z_0)^2 \\
z_1(r) &= \gamma\left[R_c - \sqrt{R_c{}^2 - r^2}\right] \\
z_2(r) &= z_1(r) + \gamma\tau \\
R_c &= \text{Radius of curvature of beam in the laboratory frame} \\
H &= \text{Beam radius} \\
\tau &= \text{Beam width} \\
\rho &= \frac{Q}{\pi H^2\gamma\tau} \\
Q &= \text{Total charge in the bunch} \\
\frac{1}{4\pi\epsilon_0} &= 9\times 10^9\left(\frac{\mathrm{V-m}}{\mathrm{coul}}\right) \quad .
\end{aligned}
$$

For a flat beam, the above solutions still apply if we just replace the integration limits for z-dimension by $z_1(r) = 0$ and $z_2(r) = \gamma\tau$. Please note these solutions do not take the image charges behind the photocathode into account.

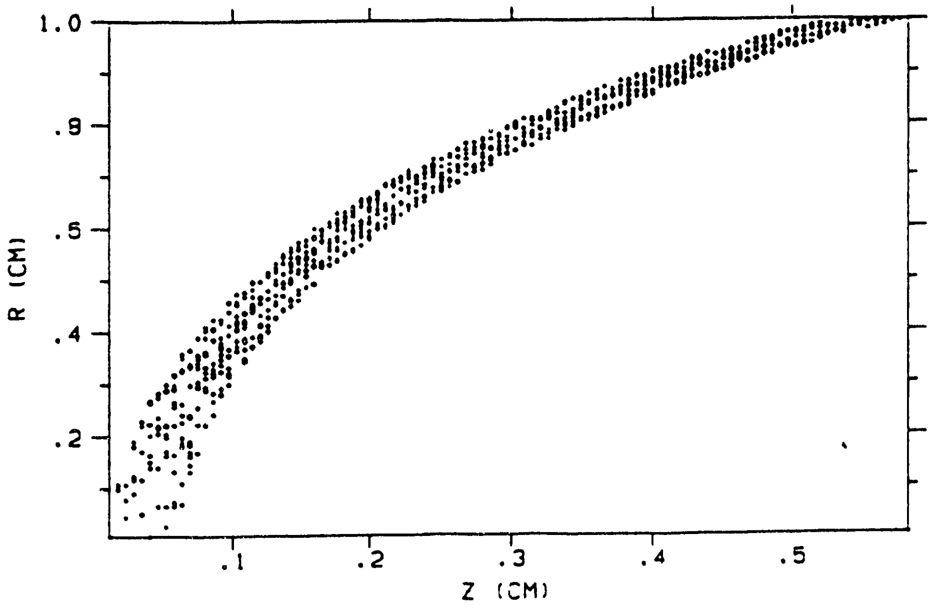

Figure 3.3.1: A pure drifting beam with cylindrically symmetric charge distribution. It is used in the estimation of the space charge forces for simplicity.

Equations (2) and (3) were evaluated numerically by an integration subroutine. The result was first checked against a well known case. For a flat beam, if we take the ratio, τ/H, to be very large then from Gauss's law we have $E'_r(r_0, \pi/2, \tau/2) = (\rho r_0)/(2\epsilon_0)$. On the other hand, if $\tau/H \lll 1$, we have $E'_z(0, \pi/2, 0) = (\rho\gamma\tau)/(2\epsilon_0)$. The numerical results agree very well with these limiting cases.

Now let's compare the numerical results with PARMELA simulations. The beam parameters we used for comparison are: $\gamma = 1.667$ ($\beta = 0.8$), $\tau = 0.06$ cm, $H = 1$ cm, $Q = 100$ nC, and $R_c = 1.2354$ cm (corresponding to a sagitta of 0.51 cm = 17 ps). Table 3.3.1 shows the the results of E'_z, while Table 3.3.2 is for E'_r.

Table 3.3.1: Longitudinal space charge fields $E'_z(0, \pi/2, 0)$ (MV/m).

E'_z	Flat Beam	Curved Beam
Analytic	17.10	24.13
PARMELA	16.30	22.26

Table 3.3.2: Radial space charge fields $E'_r(H, \pi/2, \tau/2)$ (MV/m).

E'_r	Flat Beam	Curved Beam
Analytic	22.51	12.07
PARMELA	20.49	11.27

We also modified PARMELA to simulate the image charge effect near the photocathode. The simulation results of Table 3.3.1 change to 32.87 MV/m and

41.09 MV/m for flat and curved beam respectively, when image charge effect is included in PARMELA. The longitudinal space charge field is bigger for the curved beam than for the flat beam. This is because there are more longitudinal field components toward the observation point, $(0, \pi/2, 0)$, in the curved beam than in the flat beam. Also from Table 3.3.2, we do find the radial space charge field is highly reduced for the curved beam as expected.

We used relativistic dynamics and Lorentz transformations to calculate the beam envelopes for a drifting beam ($v = 0.8\ c$) due to the transverse space charge fields which are calculated from equation (3). The result for flat beam is compared to the PARMELA simulation (without longitudinal space charge forces) in Fig. 3.3.2. They agree with each other very well.

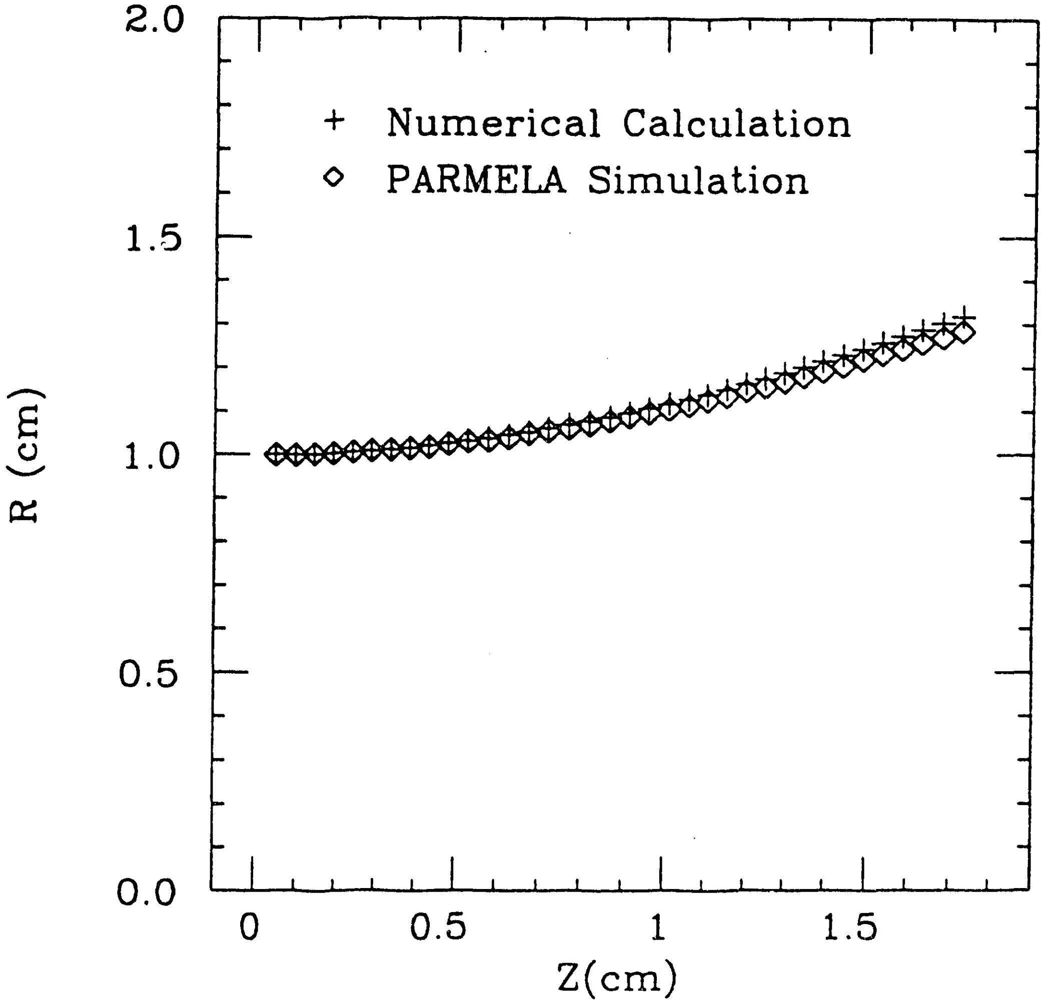

Figure 3.3.2: Comparison of beam envelopes for a drifting flat beam between the analytic calculation and the PARMELA simulation (only turn on transverse space charge forces).

3.4 OPTIMIZATION PROCEDURES

In order to get optimum parameters for the operation of the AWA, the following procedures were followed.

There are five variables used to optimize the beam quality. First is the sagitta of the beam, which can be varied through the motion of the stepper motor of the laser pulse shaper as described in the previous chapter. The main function of sagitta is to control the final bunch length. It also affects the energy spread and the total charge contained within a tolerable emittance. We will come back to this point in the next section.

Then there are two 'knobs' corresponding to electron injection rf phases at the photocathode of the gun and the entrance of the preaccelerator. They are basically used to control the output beam energy and the momentum spread.

The final two knobs belong to the fields of two solenoids. They control the beam optics and the output beam size.

In the simulation, we first choose a sagitta for the curved beam. Then the injection rf phases are chosen to maximize the output beam energy. The magnitude of the first solenoidal magnetic field between the gun and the preaccelerator is kept as small as possible to reduce the effect of chromatic aberration due to the momentum spread of the beam, but is still large enough to contain all the electrons within the aperture of the preaccelerator so that there are no losses of electrons inside the preaccelerator. Therefore the beam envelope is almost parallel to the axis after the first solenoid and the beam radius is fairly big, just slightly smaller than the aperture (5 cm). Such a big beam size also helps to relieve the space charge forces within the bunch. The beam energy has reached 10 MeV when it passes through the second solenoid. The magnitude of the second solenoid field in the middle of preaccelerator is adjusted to focus the beam toward the axis and get the desired beam size at the waist position located after the preaccelerator. Its magnitude can be roughly estimated from the focal length formula of a magnetic lens[47,48]:

$$f = \frac{4(B\rho)^2}{\int B^2 dz} \simeq \frac{4(B\rho)^2}{(B_{ave})^2 L} \quad , \tag{4}$$

where

f = Focal length

$B\rho$ = Magnetic rigidity of the beam = $3.33\, p\, (\frac{\text{GeV}}{\text{c}})$

p = Momentum of the beam in unit of (GeV/c)

B_{ave} = Average magnetic field over solenoid length L .

Since the beam is almost parallel to the longitudinal axis before entering the second solenoid, the focal length is approximately the distance from the second solenoid to the waist position we choose. The momentum of the beam is around 0.01 (GeV/c) at the second solenoid. Therefore the average magnetic field can be estimated before fine tuning with simulation.

3.5 SIMULATION RESULTS AND DISCUSSION

In this section, we are going to show the simulation results and discuss their implications. First, a typical example of working parameters for the operation of

AWA will be illustrated. Then three different effects around the operating regime will be discussed: the effect of the sagitta of the beam, and the effects of jitter in laser intensity and timing.

3.5.1 AWA OPERATING PARAMETERS

Here we present one example of an optimized set of beam parameters which can be used in the operation of AWA. The input conditions for the simulation are listed in Table 3.5.1. Figure 3.5.1 shows the beam distribution in real space (R vs Z) near the photocathode. The simulation results at the exit of the gun are shown in Fig. 3.5.2. Figure 3.5.3 shows the results at the exit of the preaccelerator. Both figures contain 4 plots: the real space beam distribution (R vs Z) is in the upper left plot, the lower left shows the Z-distribution of the number of particles, the transverse phase space (X' vs X) is shown in the upper right, and the lower right plots the longitudinal phase space (E vs Z). We also summarize the beam parameters at exits of gun and preaccelerator in Table 3.5.2.

Table 3.5.1: Input parameters for simulation.

Sagitta of Laser Pulse (ps)	17.0
Laser Pulse Width (ps)	2.0
Laser Spot Radius (cm)	1.0
Total Charge per Bunch (nC)	100
Injection rf Phase (degree)	47
Initial Kinetic Energy (eV)	1.0
Electric Field on Cathode (MV/m)	92
Peak B-Field on Axis - First Solenoid, B_1 (Gauss)	1343
Peak B-Field on Axis - Second Solenoid, B_2 (Gauss)	2299
Number of Macro Particles in Simulation	998
Time Step Size in Simulation (ps)	0.2

Table 3.5.2: Beam parameters at exits of gun and preaccelerator.

Parameters	Gun	Preaccelerator
rms Bunch Length, z_{rms} (mm)	1.91	2.87
Average Kinetic Energy, E_{ave} (MeV)	1.693	19.804
full width Energy Spread, ΔE_{fw} (MeV)	0.645	0.704
rms Transverse Emittance, $\epsilon_{x,rms}$ (mm-mrad)	100.222	18.461
Beam Radius (mm)	17.73	5.94
Total Charge in Bunch (nC)	100	100

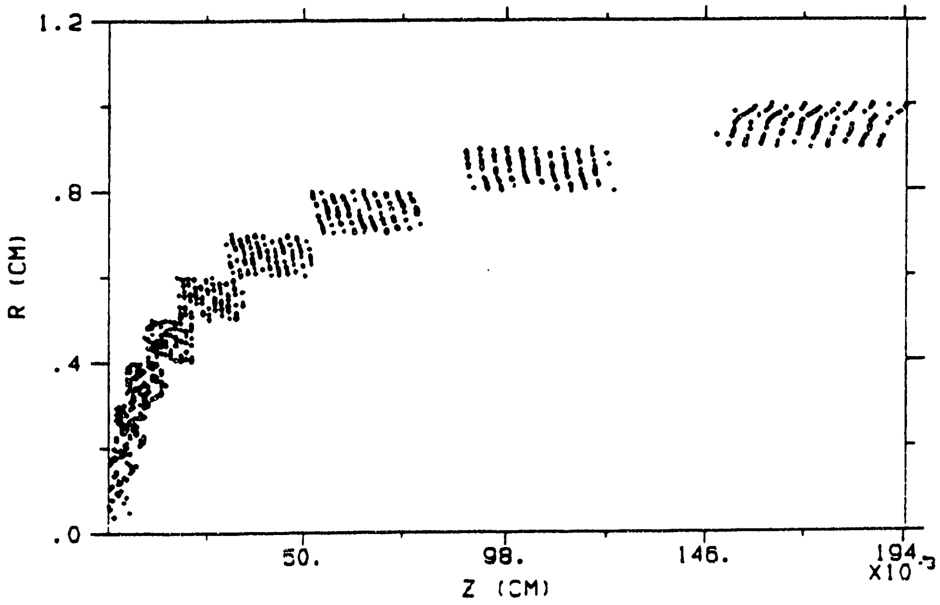

Figure 3.5.1: Initial beam distribution in real space (R vs Z) near the photocathode. R is the radius and Z is the distance from the cathode surface.

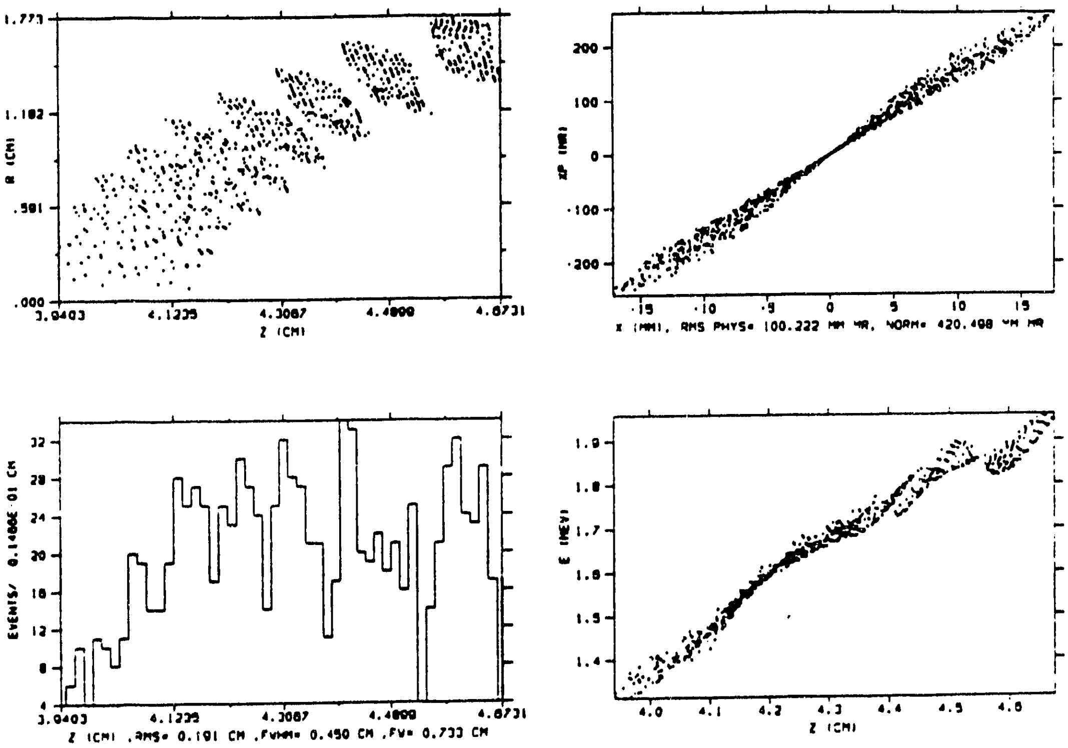

Figure 3.5.2: Beam dynamics simulation results at the gun exit. The real space beam distribution (R vs Z) is in the upper left plot, the lower left shows the Z-distribution of the number of particles, the transverse phase space (X' vs X) is shown in the upper right, and the lower right plots the longitudinal phase space (E vs Z).

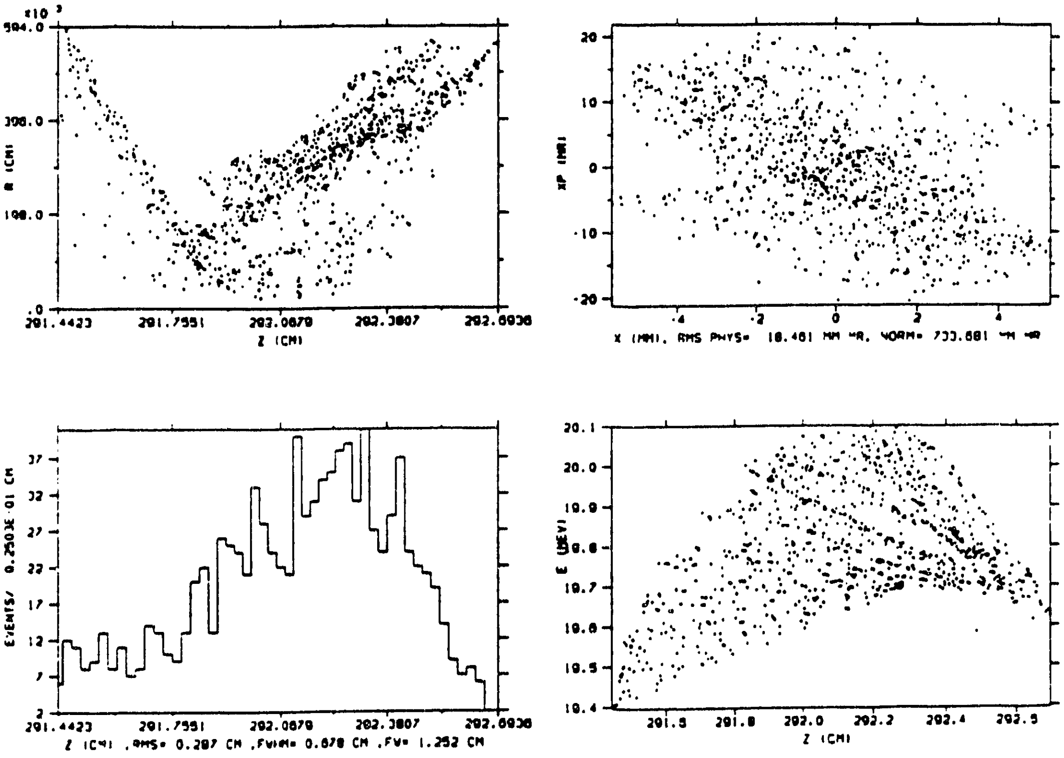

Figure 3.5.3: Beam dynamics simulation results at the preaccelerator exit. The real space beam distribution (R vs Z) is in the upper left plot, the lower left shows the Z-distribution of the number of particles, the transverse phase space (X' vs X) is shown in the upper right, and the lower right plots the longitudinal phase space (E vs Z).

At the exit of preaccelerator, as we see from Table 3.5.2, the rms bunch length is 2.87 mm ($\simeq$ 9.57 ps) for 100 nC charge with a beam radius of 5.94 mm. The full width fractional energy spread is 3.55% (= 0.704/19.804), while the rms fractional energy spread is about 0.74% (= 0.147/19.804). The rms physical emittance is 18.461 mm-mrad. Let's make a rough argument to judge the usefulness of the beam with this emittance. From Fig. 3.5.3, the full physical emittance is $\epsilon \lesssim 120$ mm-mrad, and the beam radius at the waist position is around $r_0 = 0.6$ cm. Therefore the beta function at the waist is

$$\beta_0 = \frac{{r_0}^2}{\epsilon} = \frac{36 \times 10^{-6}}{120 \times 10^{-6}} = 0.3\,\mathrm{m} \quad . \tag{5}$$

After the beam drifts a distance L from the waist, the beta function becomes

$$\beta = \beta_0 + \frac{L^2}{\beta_0} \quad . \tag{6}$$

When the beam radius blows up to $2r_0$ after drifting a distance L from the waist, the beta function is increased to $\beta = 4\beta_0$ since the emittance is roughly a constant. Thus the distance L can be calculated from eq. (6) to be $\sqrt{3}\beta_0 = 0.52$ m. On the other hand, let's take a dielectric wakefield tube with inner radius being $2r_0 = 1.2$ cm. The longitudinal wakefield generated by 100 nC beam in this tube will be around 50 MV/m.[49,50] That means the 20 MeV drive beam will transfer all its energy to the wakefield structure within a distance of 0.4 m before the beam is intercepted by the wall of the wakefield tube. Therefore, this beam is useful for the wakefield acceleration experiments even without any external focusing elements to control the beam size.

The beam parameters listed in Table 3.5.2 are roughly comparable to the operational beam qualities of the AATF except the total charge in a bunch is 100 nC for the AWA instead ~ 2 nC for the AATF. The above example provides a useful set of operation parameters for the AWA.

3.5.2 THE EFFECT OF SAGITTA

As we mentioned before, the sagitta of a concave shape beam is mainly used to control the bunch length and reduce the radial space charge forces in the early stage when the beam is still near the photocathode. If the sagitta is too short, the electrons in the outer radii tend to lag behind those of inner radii. On the other hand, if the sagitta is too long, the electrons in the inner radii will never catch up with those of outer radii.

In addition to the above phenomenon, the sagitta also plays a subtle role in reducing the energy spread. When we try to maximize the output beam energy at the exit of gun, we find the optimized injection rf phase is on the rising side of a sinusoidal wave (around 50 degrees). Therefore the outer electrons ,which are emitted earlier, experience the rf at smaller phases than the inner electrons. On the other hand, there is a correlation between the energy and radius, and also between the radius and the longitudinal position as can be recognized from the longitudinal phase space plot in Fig. 3.5.2. This is because the electric field is bigger for larger radii due to the cavity geometry. Thus the injection rf phase for inner electrons is larger for a longer sagitta bunch than for a shorter one, and hence helps more to overcome energy correlations. Therefore, a longer sagitta beam can help reduce more energy spread. We compare the full width energy spread of four different sagittas: 17 ps, 12 ps, 7 ps, and the flat beam in Table 3.5.3. The input parameters are the same as those of Table 3.5.1 except the injection rf phases are 49° for all four cases. We see a gradual reduction in energy spread as the sagitta becomes longer.

After the injection rf phases are optimized for maximum beam energy at exit of gun, we also find the phase is smaller for longer sagitta. This may be due to the fact that shorter sagitta bunch spends less time in traveling through the gun cavity and thus desires higher rf phase to gain maximum energy. This effect again favors the longer sagitta for smaller energy spread since it spends more time on the rising side of the sinusoidal wave. The results are summarized in Table 3.5.4.

Furthermore, the angular divergence of the beam is larger for a shorter sagitta bunch than a longer one. Therefore we need more magnetic field from the first solenoid to contain the beam within the aperture of the preaccelerator. This makes the chromatic effect more prominent for a shorter sagitta bunch. Table 3.5.5 shows the beam radius at exit of gun and the magnetic field used for different sagitta. Figure 3.5.4 plot several particles' trajectories through the preaccelerator. The outermost trajectory is the beam envelope. There are four plots corresponding to four different sagittas. As we expected, lower energy electrons get more over focused from the the first solenoid for a shorter sagitta bunch. Those electrons bounce outward from their shorter waist position and produce a bigger beam size at the exit of the preaccelerator. It's then necessary to use a collimator after the preaccelerator to chop the beam to the desired size. The beam contained in a given radius has less charge for a shorter sagitta bunch, but on the other hand, it has a shorter bunch length. It's a compromise among the bunch length, emittance, and total charge. Table 3.5.6 compares the beam parameters of these four sagittas at exit of preaccelerator with an aperture of 0.6 cm used to tailor the beam size.

Table 3.5.3: Energy spread of different sagittas at gun exit.

Sagitta (ps)	17	12	7	Flat Beam
Injection rf Phase (degree)	49	49	49	49
Average Kinetic Energy, E_{ave} (MeV)	1.6923	1.6857	1.6754	1.6681
Energy Spread, ΔE_{fw} (MeV)	0.655	0.668	0.704	0.772

Table 3.5.4: Energy spread of different sagittas with optimized rf phase.

Sagitta (ps)	17	12	7	Flat Beam
Injection rf Phase (degree)	47	48	49	50
Average Kinetic Energy, E_{ave} (MeV)	1.6930	1.6859	1.6754	1.6683
Energy Spread, ΔE_{fw} (MeV)	0.645	0.664	0.704	0.775

Table 3.5.5: Beam radius and magnetic fields for different sagittas.

Sagitta (ps)	17	12	7	Flat Beam
First Solenoid, B_1 (Gauss)	1343	1369	1396	1414
Beam Radius at Gun Exit (mm)	17.73	18.00	18.30	18.75

Table 3.5.6: Beam parameters for different sagittas at preaccelerator exit.

Sagitta (ps)	17	12	7	Flat Beam
z_{rms} (mm)	2.87	2.51	2.17	2.30
E_{ave} (MeV)	19.804	19.778	19.749	19.680
ΔE_{fw} (MeV)	0.704	0.725	0.775	0.999
$\epsilon_{x,rms}$ (mm-mrad)	18.461	19.778	20.081	23.540
Beam Radius (mm)	5.94	5.94	5.97	6.00
Total Charge (nC)	100	95.591	89.178	57.615

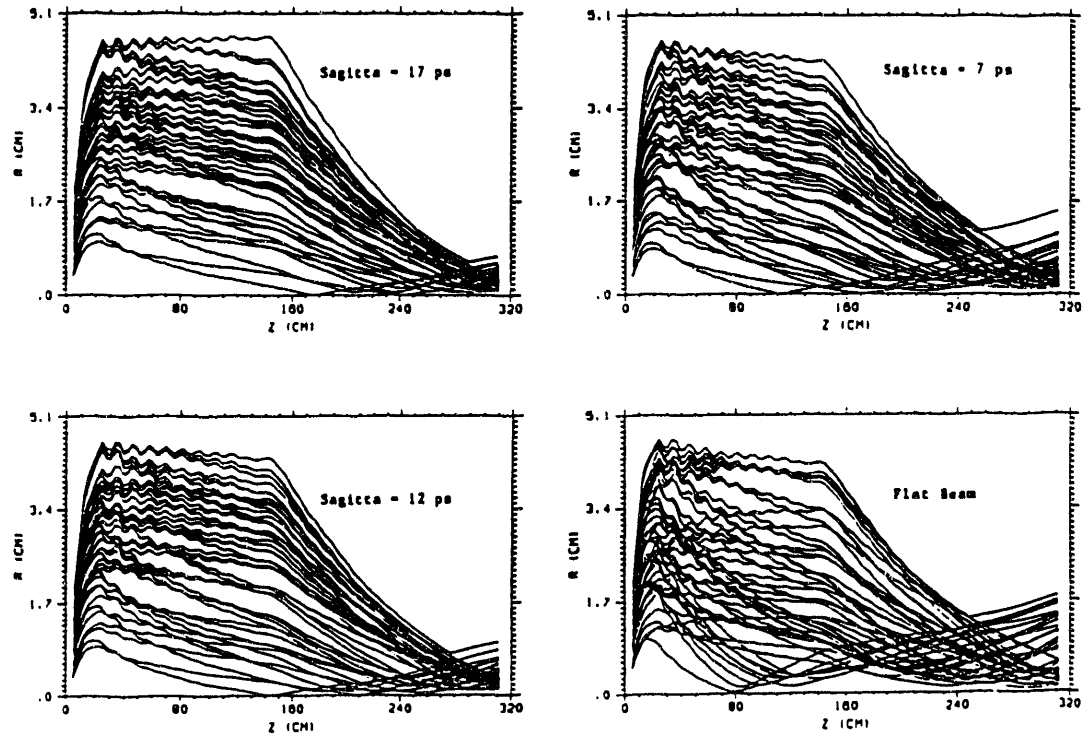

Figure 3.5.4: Ray-traces (gun through preaccelerator) of the drive beam. R is the radius and Z is the distance from the cathode surface. There are four plots corresponding to four sagittas: 17 ps (upper left), 12 ps (lower left), 7 ps (upper right) and flat beam (lower right).

3.5.3 LASER AMPLITUDE JITTER EFFECT

As pointed out in the last chapter, an initial study of the AWA laser system indicates the amplitude jitter of the laser intensity is $\leq$ 13% (p-p). An amplitude noise suppressor is under development.[51] In this section we consider the effect of the amplitude jitter on the beam dynamics.

The laser amplitude directly controls the total charge emitted from the photocathode. The nominal operating value of the total charge out of the laser photocathode is 100 nC. We are going to investigate the effect of variations ±10% of the nominal charge.

All the input conditions are the same as those in Table 3.5.1, except the total charge out of the photocathode. Table 3.5.7 and Table 3.5.8 summarize the beam parameters at the exits of gun and preaccelerator respectively.

As we expect, the energy spread is bigger for more charge in a bunch due to the space charge and the wakefield effects. Therefore, 110 nC beam suffers most chromatic effect from the first solenoid. However, after we collimate the beam radius to be around 0.6 cm, there is still 107 nC left in the bunch although its emittance and bunch length is a little worse than the 100 nC bunch.

Table 3.5.7: Beam parameters for different charges at gun exit.

Charge Out of Cathode (nC)	90	100	110
z_{rms} (mm)	1.83	1.91	1.99
E_{ave} (MeV)	1.710	1.693	1.677
ΔE_{fw} (MeV)	0.596	0.645	0.707
$\epsilon_{x,rms}$ (mm-mrad)	88.252	100.222	111.753
Beam Radius (mm)	17.55	17.73	17.91

Table 3.5.8: Beam parameters for different charges at preaccelerator exit.

Charge Out of Cathode (nC)	90	100	110
z_{rms} (mm)	2.56	2.87	3.09
E_{ave} (MeV)	19.800	19.804	19.807
ΔE_{fw} (MeV)	0.613	0.704	0.810
$\epsilon_{x,rms}$ (mm-mrad)	16.275	18.461	19.968
Beam Radius (mm)	5.28	5.94	5.97
Charge Left in Bunch (nC)	90	100	107.024

3.5.4 LASER TIMING JITTER EFFECT

The initial study of the AWA laser system also indicates the timing jitter of the laser is ≤ 5 ps. For a L-band rf cavity, this corresponds to about $\Delta\phi = 2.34°$ in rf phase since $\Delta\phi = 360 f \Delta t$ with $f = 1.3$ GHz and $\Delta t = 5$ ps. In this section, we are going to study ±2° out of the optimized injection rf phase for the 17 ps sagitta beam, i.e., 45° and 49°.

All the input conditions are the same as those in Table 3.5.1, except the injection rf phases. Table 3.5.9 and Table 3.5.10 summarize the beam parameters at the exits of gun and preaccelerator respectively.

As we already explained before, a smaller injection rf phase means the bunch spends more time on the rising side of the sinusoidal wave and hence reduces more energy spread. However, the variation of beam quality is still within tolerable limits as can be seen from Table 3.5.10.

Table 3.5.9: Beam parameters for different rf phases at gun exit.

Injection rf Phase (degree)	45	47	49
z_{rms} (mm)	1.91	1.91	1.90
E_{ave} (MeV)	1.692	1.693	1.692
ΔE_{fw} (MeV)	0.633	0.645	0.655
$\epsilon_{x,rms}$ (mm-mrad)	100.053	100.222	100.606
Beam Radius (mm)	17.58	17.73	17.88

Table 3.5.10: Beam parameters for different rf phases at preaccelerator exit.

Injection rf Phase (degree)	45	47	49
z_{rms} (mm)	2.87	2.87	2.89
E_{ave} (MeV)	19.711	19.804	19.875
ΔE_{fw} (MeV)	0.592	0.704	0.845
$\epsilon_{x,rms}$ (mm-mrad)	17.920	18.461	19.033
Beam Radius (mm)	5.52	5.94	6.36
Charge Left in Bunch (nC)	100	100	99.699

4 Experimental Investigations

We conducted a series of low power level rf measurements on the gun cavity and the preaccelerator. Several methods for tuning the cavity frequency are discussed and results are presented. We also measured the quality factor of the gun cavity and the result is compared to that calculated from URMEL. The effect of field asymmetry due to the rf coupling iris in the side wall of the cavity and the laser spot misalignment problem are investigated. The preliminary high power tests of the gun cavity are discussed.

4.1 MEASUREMENT AND TUNING OF CAVITY FREQUENCY

A network analyzer (HP 8510) was used for low power level bench measurements. The HP 8510 network analyzer system is an advanced and sophisticated measuring instrument designed to make microwave measurements of many kinds. The basic principles of its operation are fairly simple. The network analyzer system consists of four essential parts: (1) a source, (2) a test set, (3) a signal detector and analog-to-digital converter, and (4) a digital microprocessor and display. The source provides the rf signal. The test set separates this signal into an incident signal sent to the device under test and a reference signal against which the transmitted and reflected signals are later compared. It also receives transmitted and reflected signals from the device under test. The signal detector and analog-to-digital converter takes all of these signals and converts them to digital information for high speed processing. The digital microprocessor controls the system, analyzes the digitized signals, corrects errors, and displays the results in a variety of formats. Figure 4.1.1 shows the block diagram of this system.

The resonant frequencies of the cavity can be obtained by the reflection coefficient measurement from the network analyzer. The rf signal was coupled into the copper cavity through an elliptical shape hole on the top of the cavity. The coupling iris was covered by an L-band WR-650 waveguide. A 50Ω coaxial cable was connected from port 1 of the network analyzer to a waveguide-to-coax adaptor, which was attached to the WR-650 waveguide.

A network analyzer measurement of the reflection coefficient for the gun cavity is shown in Fig. 4.1.2. Figure 4.1.3 shows a comparison of the measured dispersion curve for a four cell prototype cavity of the preaccelerator with the URMEL predictions. Excellent agreement with the parameters as computed by URMEL is obtained.

It is well known that a resonant cavity can be thought of as an L-C circuit where L and C are the equivalent inductance and capacitance of the cavity, respectively. Thus the resonant frequency f_0 of the cavity can be expressed as $f_0 = 1/(2\pi\sqrt{LC})$. The thermal expansion of the cavity due to a rise in temperature will change both the inductance and capacitance, and as a result the resonant frequency of the cavity shifts. To first order of approximation, the following relation between frequency and temperature holds[52]:

$$\frac{\Delta f}{f} = -\nu \Delta T \tag{7}$$

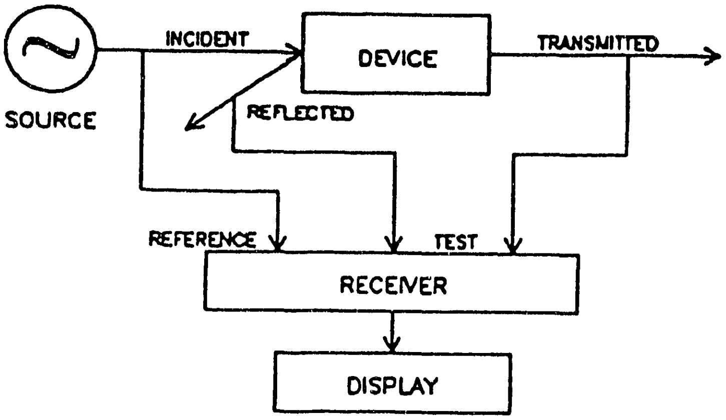

Figure 4.1.1: Block diagram of the HP 8510 network analyzer system.

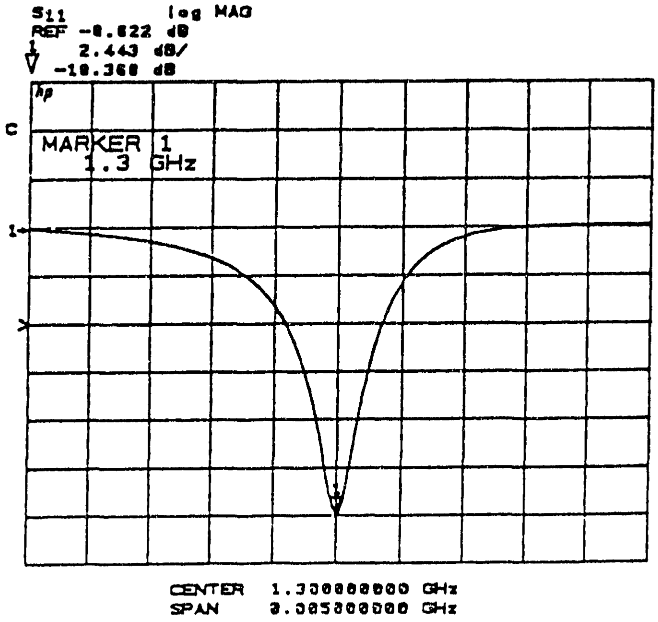

Figure 4.1.2: Measured reflection coefficient of the gun cavity.

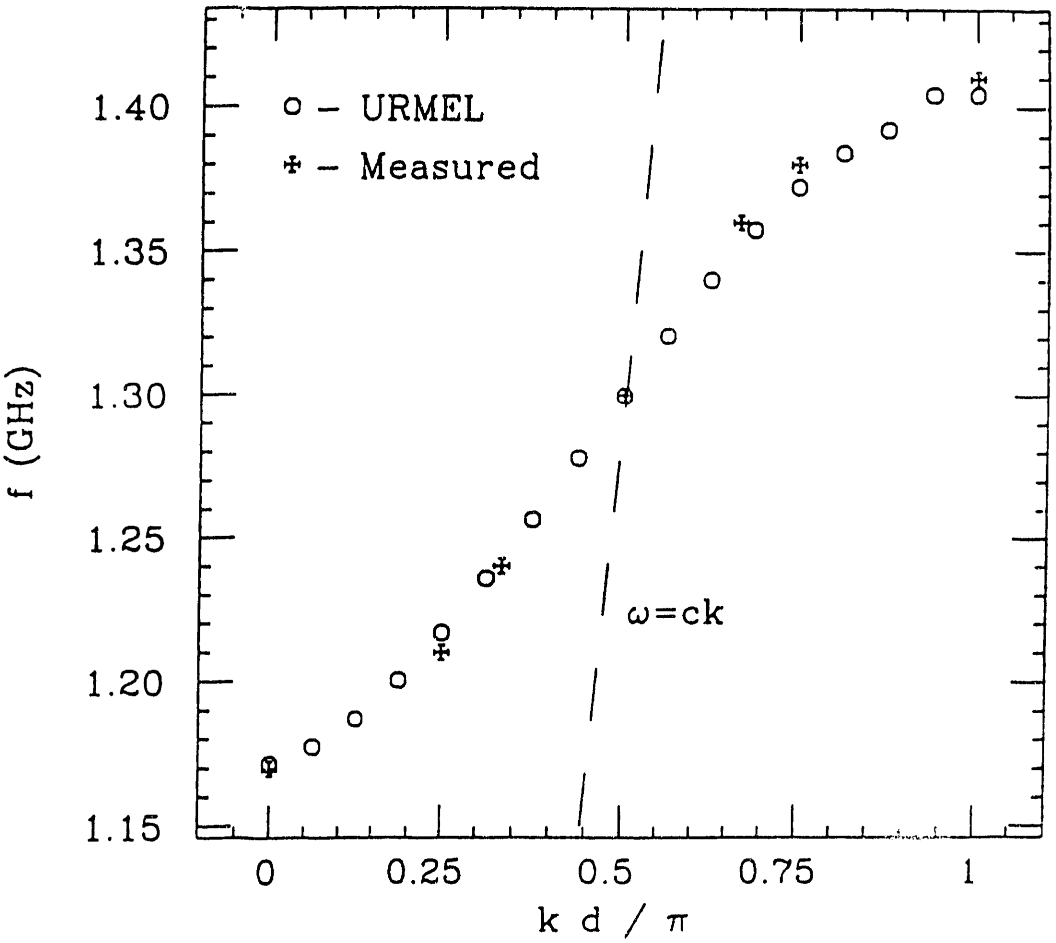

Figure 4.1.3: Comparison of the measured dispersion curve with URMEL calculations for the preaccelerator cavity.

where

$$\begin{aligned}
\Delta f &= f - f_0 = \text{change of frequency} \\
\Delta T &= T - T_0 = \text{change of temperature} \\
\nu &= \text{coefficient of linear thermal expansion} \\
&= 1.6 \times 10^{-5}/^{\circ}\mathrm{C} \quad \text{for copper}
\end{aligned}$$

We did bench measurements on this temperature-frequency relation for the rf gun cavity. The experimental setup is shown schematically in Fig. 4.1.4. A laboratory 'hot plate' with input power adjusted by a variable auto transformer (VARIAC) was used to heat the copper cavity from room temperature to about 30 °C. The temperature of the cavity was monitored by an HP 2840A Quartz Thermometer. The HP 2804A temperature sensor is a quartz crystal whose precise angle of cut gives a stable and repeatable relationship between resonant frequency and temperature. Its performance range is from −80 to 250°C and three levels of resolution can be selected: 0.01, 0.001, and 0.0001 °C. The frequency of the cavity was measured using the HP 8510 Network Analyzer. Both frequency and temperature measurements were controlled by the HP 85 Personal Computing System in which programs were written in BASIC to take the data every minute, store them on the floppy disk, and plot them using the HP 7470A plotter.

The measurement result of frequency versus temperature for the first prototype gun cavity is presented in Fig. 4.1.5, where the slope is approximately $\Delta f/\Delta T \sim (1161667.7 - 1161784.7)/(30.92 - 24.50) = -18.2$ KHz/°C. This is in excellent agreement with the predicted value of −18.6 KHz/°C from eq. (7).

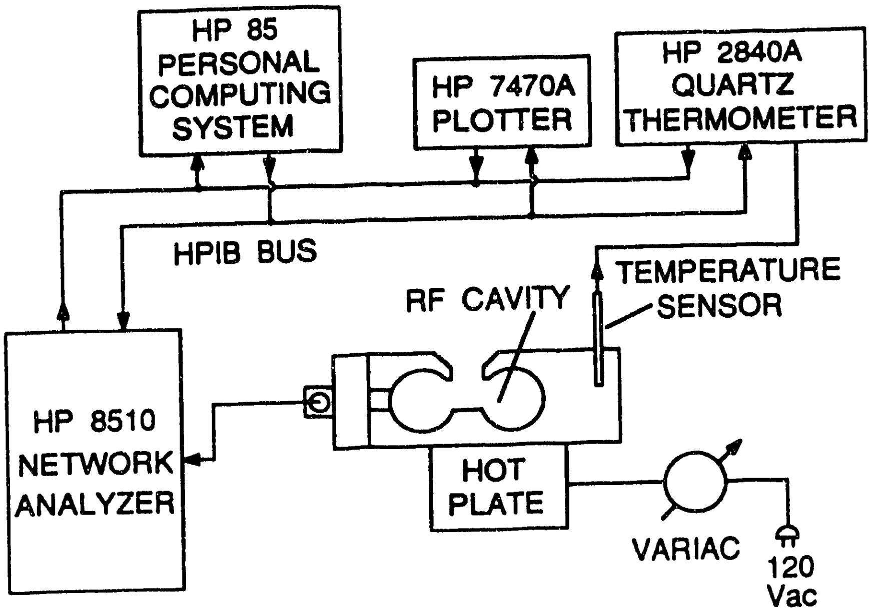

Figure 4.1.4: The Schematic of the frequency-temperature measurement setup.

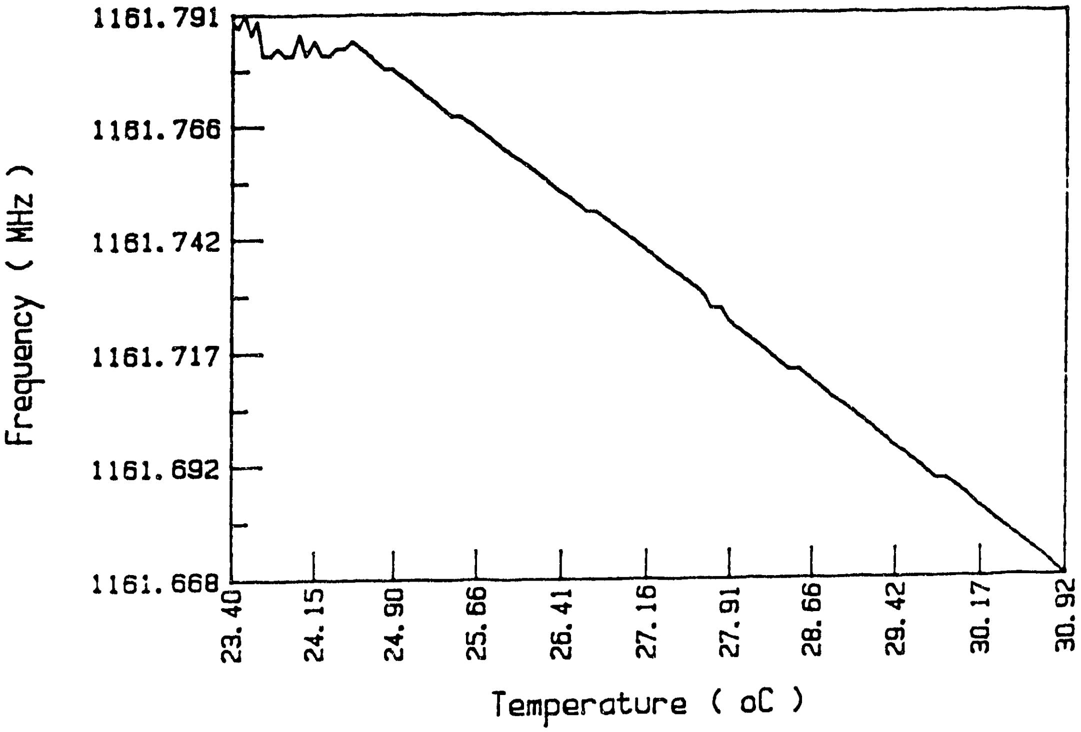

Figure 4.1.5: Measured frequency response as a function of temperature.

In regard to evacuating the cavity, the capacitance is proportional to the dielectric constant ϵ of its filling media. Therefore we expect the following relation between the dielectric constant and the frequency:

$$\frac{f_1}{f_2} = \sqrt{\frac{\epsilon_2}{\epsilon_1}} \quad . \tag{8}$$

The dielectric constant of air at standard temperature and pressure is 1.0005364,[53] while it is 1.0 for vacuum. The resonant frequency of the cavity will thus shift up when the air inside the cavity is pumped out.

The operating temperature for the gun cavity will be 90°F, while the room temperature is 78°F. Using equations (7) and (8), we can figure out that the resonant frequency in air at room temperature should be 1299.8 MHz if we desire the operating frequency to be 1300 MHz.

The fine tuning of the resonant frequency for the gun cavity can be achieved by the adjusting the position of the photocathode plug. Since the cathode plug is located in the strong electric field region, the equivalent cavity capacitance will be changed when the depth of the cathode plug penetration into the cavity is adjusted. The capacitance will be increased by increasing the penetration of the cathode plug, and hence the resonant frequency can be reduced. The bench measurement result is shown in Fig. 4.1.6, where the zero plug position represents the cathode plug is aligned with the inner surface of the cavity while more negative position means the plug penetrates more into the cavity. The plug position can adjust the frequency at a rate of $\sim$ 3 MHz/mm as estimated from Fig. 4.1.6.

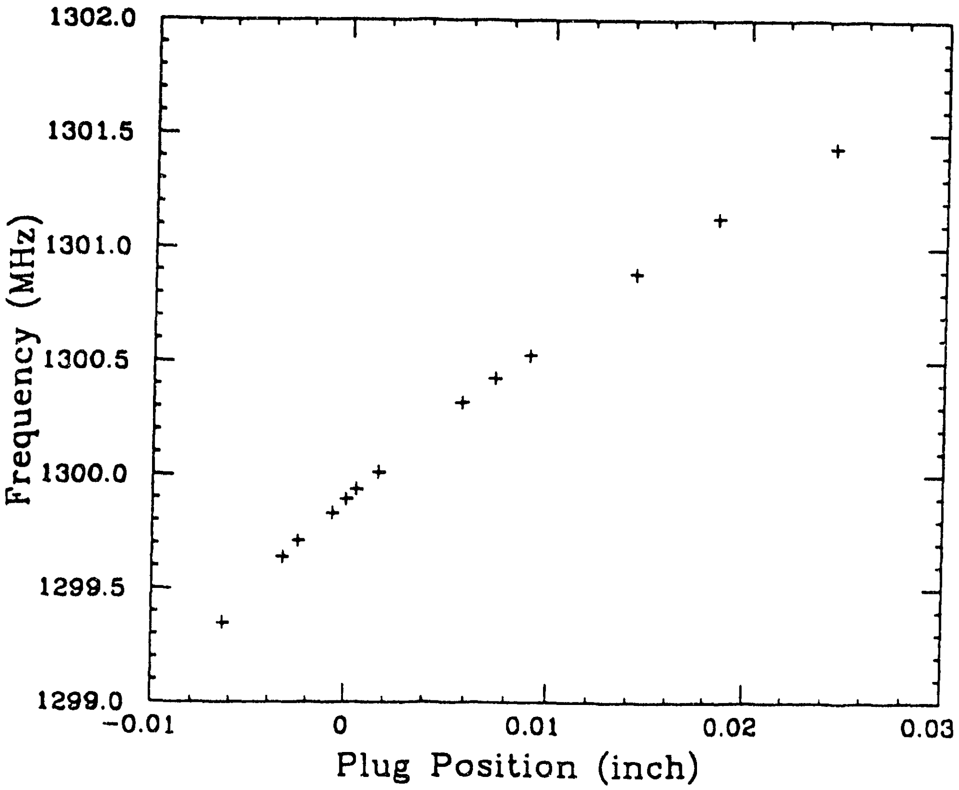

Figure 4.1.6: Measured frequency vs cathode plug position.

The frequency tuning operation for the preaccelerator consists of indenting the walls of each cavity with four small dimples located at 90° about the axis. A precision press system is available to exert forces to indent the walls.

4.2 MEASUREMENT OF QUALITY FACTOR

The quality factor Q of the cavity is defined as the ratio of the stored energy to the energy lost in one radian of an oscillation. In the steady state, the rf generator supplies power losses in cavity walls to maintain the fields inside the cavity. If the generator also supplies power to elements external to the cavity, it should be included in the calculation of Q. We define Q_0 as the quality factor of the cavity unloaded by the external elements. Thus the unloaded quality factor Q_0 is

$$Q_0 \equiv \frac{\omega_0 U}{P_{cavity}} \quad , \tag{9}$$

where $\omega_0 = 2\pi f_0$, f_0 is resonant frequency of the cavity, U is the stored energy of the cavity, and P_{cavity} is the average power dissipated on the cavity walls. The total (loaded) power supplied by the rf generator is

$$P_T = P_{cavity} + P_{external} \quad . \tag{10}$$

If the loaded quality factor is defined as

$$Q_L \equiv \frac{\omega_0 U}{P_T} \quad , \tag{11}$$

then

$$\frac{1}{Q_L} = \frac{1}{Q_0} + \frac{1}{Q_{ext}} \quad , \tag{12}$$

where

$$Q_{ext} \equiv \frac{\omega_0 U}{P_{external}} \quad . \tag{13}$$

When the cavity is coupled to a signal generator such as the rf source in the network analyzer, it can be represented by a simple series RLC-circuit, as shown in Fig. 4.2.1. The Q of the system to the right of line A-A is the unloaded quality factor Q_0 as defined above. Therefore Q_0 can be calculated as

$$Q_0 = \omega_0 \frac{\frac{1}{2} L I^2}{\frac{1}{2} r I^2} = \frac{\omega_0 L}{r} \quad , \tag{14}$$

where $(I \cos \omega_0 t)$ is the current and ${\omega_0}^2 = 1/(LC)$. Similarly, the loaded quality factor Q_L is

$$Q_L = \frac{\omega_0 L}{r + Z_0} \quad , \tag{15}$$

where Z_0 is characteristic impedance of the transmission line.

The coupling parameter β is defined as

$$\beta \equiv \frac{Z_0}{r} \quad . \tag{16}$$

When $\beta = 1$, the coupled resistance and cavity losses are equal, and the cavity is said to be critically coupled. The cavity is said to be undercoupled when $\beta < 1$, and is called overcoupled when $\beta > 1$. Using the definition of the coupling parameter β, we have the following relations between Q_L, Q_{ext}, and Q_0:

$$Q_0 = (1 + \beta) Q_L \quad , \tag{17}$$

and

$$Q_{ext} = \frac{Q_0}{\beta} \quad . \tag{18}$$

The impedance at the reference plane A-A of the equivalent circuit shown in Fig. 4.2.1 is equal to

$$Z = r + \mathrm{j}(\omega L - \frac{1}{\omega C}) = r + \mathrm{j}(\frac{\omega}{\omega_0} - \frac{\omega_0}{\omega})\sqrt{\frac{L}{C}} \quad , \tag{19}$$

where j represents the unit imaginary. For cavities with high Q_0, $\omega \approx \omega_0$. Therefore the impedance Z can be written as

$$Z \approx r + \mathrm{j}(2rQ_0\frac{\delta}{f_0}) \quad , \tag{20}$$

where $\delta \equiv f - f_0$.

The reflection coefficient ρ is defined as the ratio of the reflected voltage to the incident voltage. The return loss in dB as read from the network analyzer rectangular display is related to ρ by:

$$\text{Return loss} = 20\log_{10}\rho \quad . \tag{21}$$

The reflection coefficient at the terminal plane A-A in Fig. 4.2.1 is:

$$\rho = \frac{Z - Z_0}{Z + Z_0} = \frac{r - Z_0 + \mathrm{j}(2rQ_0\delta/f_0)}{r + Z_0 + \mathrm{j}(2rQ_0\delta/f_0)} \quad . \tag{22}$$

The magnitude of ρ is:

$$|\rho| = \sqrt{\frac{(r - Z_0)^2 + (2rQ_0\delta/f_0)^2}{(r + Z_0)^2 + (2rQ_0\delta/f_0)^2}} \quad . \tag{23}$$

When δ satisfies the following condition:

$$\left|\frac{f_0}{2\delta}\right| = \frac{Q_0}{1 + (Z_0/r)} = \frac{Q_0}{1 + \beta} = Q_L \quad , \tag{24}$$

the magnitude of ρ can be simplified to

$$|\rho| = \frac{\sqrt{1+\beta^2}}{1+\beta} \quad . \tag{25}$$

The coupling parameter β can be determined from the input impedance measurement using the network analyzer. Therefore the frequency bandwidth 2δ at the return loss from eq. (25) can be measured. The loaded quality factor can then be determined from eq. (24).

The coupling of the rf power to the gun cavity had been bench tested. It was found that the optimum configuration of the coupling hole for the gun cavity is an elliptical iris with the length of the major semiaxis being 1 inch and the minor semiaxis being 3/8 inch. Figure 4.2.2 shows the Smith chart for the impedance measurement from the network analyzer. The impedance of the transmission line is $Z_0 = 50\Omega$. The input resistance measured from Fig. 4.2.2 is $r = 46.4\Omega$. Therefore the coupling parameter is $\beta = 50/46.4 = 1.08$, which is close to critical coupling. The return loss for this β is about -3 dB. The frequency bandwidth 2δ is 212.5 KHz as shown in Fig. 4.2.3. The loaded quality factor is $Q_L =$ 1.30127 GHz/212.5 KHz = 6124. The unloaded quality factor is $Q_0 = (1 + 1.08)Q_L = 12737$. The calculated unloaded quality factor from URMEL is 15000 as listed in Table 2.3.1.

We also measured the isolation of the rf power from the gun cavity to the preaccelerator of four-cell prototype cavity. The rf signal is inputed from port 1 of the network analyzer to the gun cavity and returns from the end cell of the preaccelerator to port 2 of the analyzer. Transmission loss due to antenna coupling is --15 dB, thus the true transmission loss is -37.143 dB as can be seen from Fig. 4.2.4. Therefore the leakage of the field from the gun to the preaccelerator is not of concern.

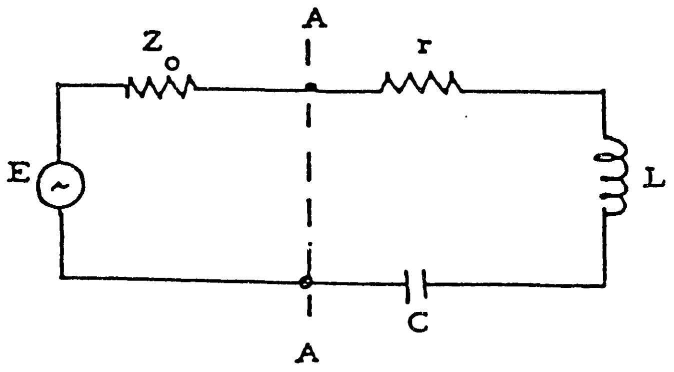

Figure 4.2.1: Equivalent circuit of cavity coupled to a signal generator.

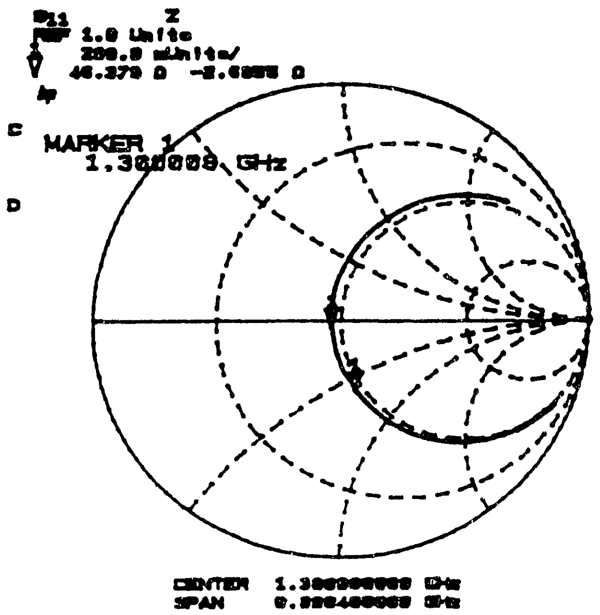

Figure 4.2.2: Smith chart for the impedance measurement.

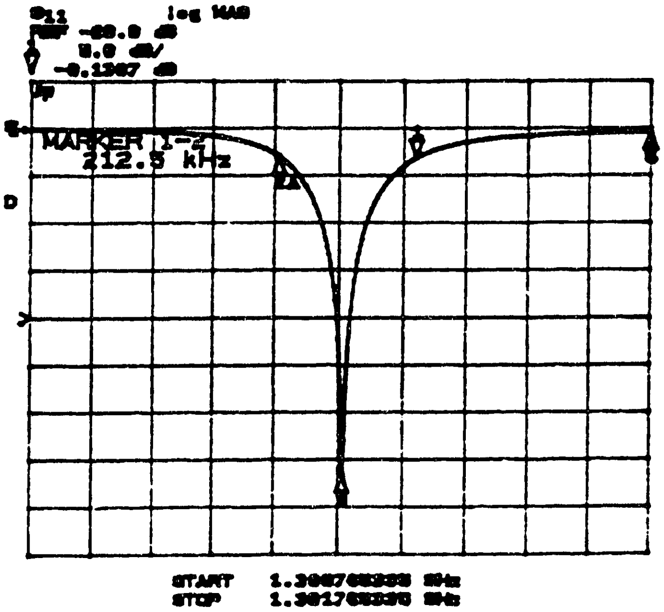

Figure 4.2.3: Measured frequency bandwidth at half-power-point.

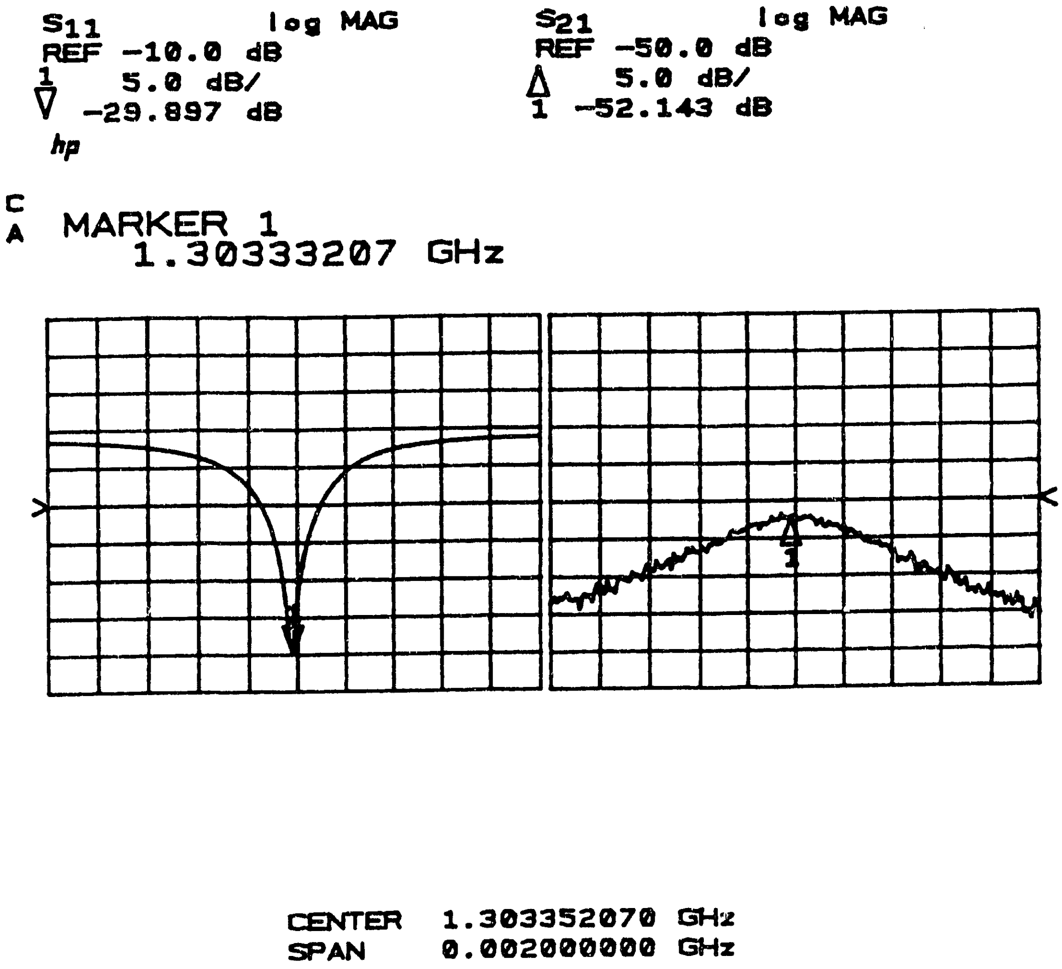

Figure 4.2.4: Measured transmission loss from gun cavity to preaccelerator.

4.3 RF FIELD ASYMMETRY AND LASER SPOT ALIGNMENT

4.3.1 INTRODUCTION

There are two independent causes of transverse beam deflection in the AWA photo-cathode cavity. The first is asymmetry of the electromagnetic fields due to the input-power coupling iris in the side wall and the second is misalignment of the laser spot on the photo-cathode surface. The magnitude of beam deflection from these two effects has been estimated and the results are presented in the following sections.

4.3.2 RF FIELD ASYMMETRY

A. Physical Description

Any rf cavity (or traveling wave section of an accelerator) has an asymmetry in its electromagnetic fields due to the coupling of rf power from an external source through an iris in the side wall of the cavity. The ideal TM_{0n} modes are perturbed by at least two contributions from a single coupling port: (1) the superposition of a dipole cavity mode due to the boundary condition imposed by the iris in the side wall, and (2) the superposition of a transversely traveling wave in the cavity which replenishes rf power (via the iris) lost to the finite-conductivity walls. The dipole perturbation can be reduced by placing a second iris on the opposing side wall of the cavity which forces the perturbation to be of a quadrupole nature. In general, the higher the multipole, the less severe the perturbation. If the second iris is an rf power feed, the traveling-wave perturbation is reduced by the symmetry of power flow. However, if the second iris is simply coupled to a shorted waveguide, the traveling-wave perturbation is enhanced since the wave has to also supply the power lost in the "balancing" cavity. In superconducting cavities, where wall losses are minimal, the traveling-wave perturbation may be negligible.

B. Fields and Particle Motion

The accelerating electric field near the cavity axis is assumed to be axially uniform and may be approximated by[54]

$$E_z \simeq \left(E_{z0} + \frac{y\Delta E}{h}\right) \sin(\omega t + \phi_0 + \frac{y\Delta\phi}{h}) \quad , \tag{26}$$

where E_{z0} is the unperturbed field of the TM_{0n} modes, ΔE is the nearly linear dipole contribution, h is the transverse distance over which the dipole field varies by ΔE in the y-direction, $\Delta\phi$ is the traveling-wave contribution which manifests itself as a phase variation in the accelerating field over the distance h, and ω and ϕ_0 are the angular frequency and initial phase of the unperturbed accelerating field. The phase perturbation $\Delta\phi$ can be understood physically by considering the illustration in Fig. 4.3.1 where two observers separated by distance Δy see the same oscillation due to the passage of a traveling wave, but with phase difference $\Delta\phi = \omega\Delta y/v_\phi$, where v_ϕ is the phase velocity of the wave. It is just such a traveling wave that passes across the photo cathode surface, giving the phase perturbation in eq. (26).

The deflecting force on a particle arises from the perturbed transverse magnetic field which is related to the axial electric field by

$$\frac{\partial B_x}{\partial t} = -\frac{\partial E_z}{\partial y} \quad , \tag{27}$$

or

$$B_x(t) \simeq \frac{E_{z0}}{\omega h}\left[A \cos(\omega t + \phi_0) - \Delta\phi \sin(\omega t + \phi_0)\right] \quad , \tag{28}$$

where $A = \Delta E/E_{z0}$ and only first order terms have been included. In equation (28), the first term is due to the dipole mode and its contribution to B_x is in quadrature with the accelerating field, as is expected for cavity modes. Since this dipole force is zero when axial acceleration is maximum ($\omega t + \phi_0 = 90°$), it is generally labeled as a head-to-tail shearing of the bunch. The second term in eq. (28) is due to the transversely traveling wave and its contribution to B_x is in phase with the accelerating field, defining the transverse Poynting vector. This force is thus labeled as a coherent kick to the entire bunch. The various forces just described are illustrated[55] in Fig. 4.3.2.

Inserting the above magnetic field into the force balance equation,

$$\frac{dp_y}{dt} = qc\beta_z(t)B_x(t) \quad , \tag{29}$$

the transverse momentum of a particle starting from rest at the photo-cathode surface is given by

$$p_y(t) = \frac{qcE_{z0}}{\omega h}\int_0^t \beta_z(\tau)\left[A \cos(\omega\tau + \phi_0) - \Delta\phi \sin(\omega\tau + \phi_0)\right] d\tau \quad , \tag{30}$$

where the axial velocity β_z is determined from the unperturbed accelerating field and is given by

$$\beta_z(t) = \frac{K(t)}{\sqrt{K^2(t) + 1}} \quad , \tag{31}$$

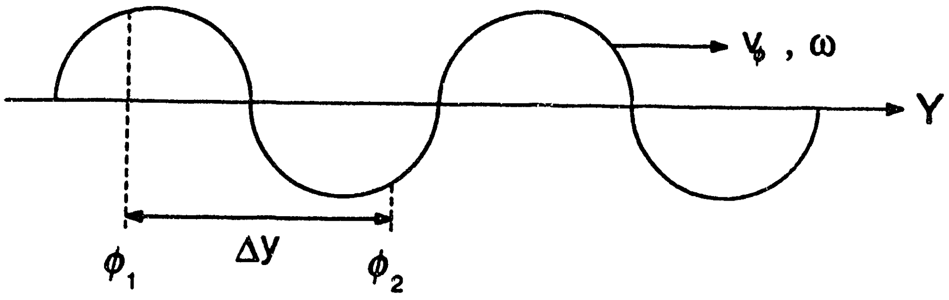

Figure 4.3.1: Illustration of phase variation due to traveling wave contribution.

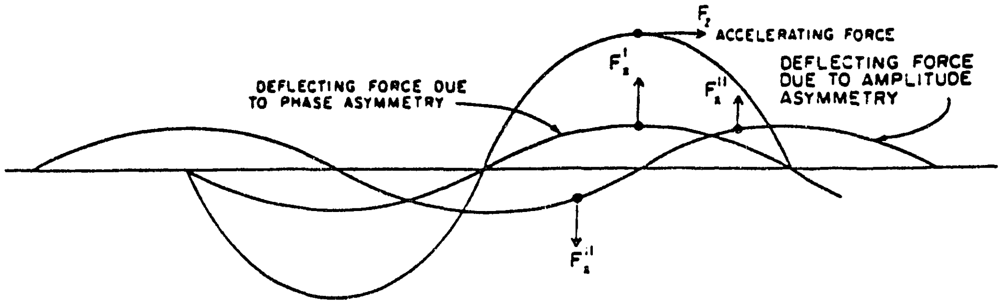

Figure 4.3.2: Force components due to amplitude and phase asymmetry in the coupler cavities.

with

$$K(t) = -\frac{qE_{z0}}{\omega mc}\Big[\cos(\omega t + \phi_0) - \cos\phi_0\Big] \quad . \tag{32}$$

The particle's axial position is then

$$z(t) = c\int_0^t \beta_z(\tau)\,d\tau \quad . \tag{33}$$

Finally, at the exit of the photo-cathode cavity the divergence of a particle originating on axis is

$$\alpha = \tan^{-1}\left(\frac{p_y}{p_z}\right) \quad , \tag{34}$$

and its transverse offset is

$$y(t) = \int_0^t \frac{p_y(\tau)}{\gamma(\tau)\,m}\,d\tau \quad . \tag{35}$$

The transverse shear of the bunch, which is of importance for emittance considerations, is simply the difference of eq. (34) evaluated for the front and back of the bunch, $\Delta\alpha = \alpha_f - \alpha_b$. When applying the above equations to a cavity or single cell of a linac with an axially non-uniform field, the variables t, E_{z0}, and, to a lesser extent, ϕ_0 have to be adjusted to agree with other estimates of exiting particle energy, axial position, and transit time.

C. Measurement Technique

The parameters of the photo-cathode cavity that have to be measured to obtain estimates of particle divergence and offset are the relative dipole perturbation, A, and phase perturbation, $\Delta\phi$. These quantities are found by observing the variation of the reflected signal from the cavity, S_{11}, as a function of the position of a small metallic or dielectric needle inside the cavity. The deviation of resonant frequency from the empty cavity value due to a needle pointing along the axis is given by[56,57]

$$\Delta f = kE_z^2 \quad , \tag{36}$$

where k is a constant depending on the needle geometry and E_z is the axial electric field strength at the position of the needle. Referring to Fig. 4.3.3, the difference in axial electric field between position 1 and position 2 is then

$$\Delta E = E_1 - E_2 = \frac{\sqrt{\Delta f_1} - \sqrt{\Delta f_2}}{\sqrt{k}} \quad , \tag{37}$$

where Δf_1 and Δf_2 are measured at each position. The unperturbed field on axis is approximately

$$E_{z0} \simeq \frac{E_1 + E_2}{2} = \frac{\sqrt{\Delta f_1} + \sqrt{\Delta f_2}}{2\sqrt{k}} \quad , \tag{38}$$

thus the parameter A is given by[58]

$$A = \frac{\Delta E}{E_{z0}} = \frac{2\left(\sqrt{\Delta f_1} - \sqrt{\Delta f_2}\right)}{\sqrt{\Delta f_1} + \sqrt{\Delta f_2}} \quad , \tag{39}$$

and the constant k need not be determined. The phase perturbation is simply given by

$$\Delta\phi = \frac{\phi_1 - \phi_2}{2} \quad , \tag{40}$$

where ϕ_1 and ϕ_2 are the respective phases of S_{11} at the two needle positions and the factor of two is due to the additional path length of the reflected signal in returning to the coupling port.

Since the unperturbed TM_{0n} modes have a B_θ field which opposes the dipole B_x field along half the y-axis (and adds to it along the other half), the dipole perturbation can be viewed as an approximate offset of the rf center of the cavity. There is a null in the transverse field when

$$B_x \simeq \frac{\partial(rB_\theta)}{r\,\partial r}\,\delta y \quad , \tag{41}$$

where δy is the offset of the rf center. Using the dipole component of equation (28) and near the cavity axis

$$\frac{\partial(rB_\theta)}{r\,\partial r} \simeq \frac{\omega E_{z0}}{c^2} \quad , \tag{42}$$

equation (41) yields

$$\delta y \simeq \frac{c^2 A}{\omega^2 h} \quad . \tag{43}$$

This value is useful when comparing the effects of coupling irises on various cavities.

Measurements of A and $\Delta\phi$ for the AWA photo-cathode cavity were performed by inserting a plug into the aperture of the cavity with a stainless steel needle extending from the normal face of the plug as shown in Fig. 4.3.4 to be parallel to the E_z field. The plug was machined to fit the aperture diameter to within 2 mil and there were three radial positions of the needle: 1/8", 1/4", and 1/2". The needle was positioned azimuthally to cross the transverse axis containing the wall iris (y-axis in Fig. 4.3.3) and rotated successively 180° after noting the resonant frequency deviation from the case with no needle in the plug for use in eq. (39). Care was taken to obtain resonant frequency reproducibility with eventual 360° rotations of the needle. This was exacerbated by the use of the aluminum prototype cavity with its inherent poor surface contact conductivity as well as the 2 mil fit of the plug into the aperture. Even more adversely affected

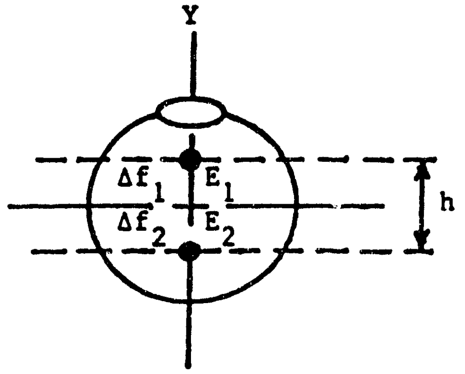

Figure 4.3.3: Illustration of the frequency perturbation measurement technique.

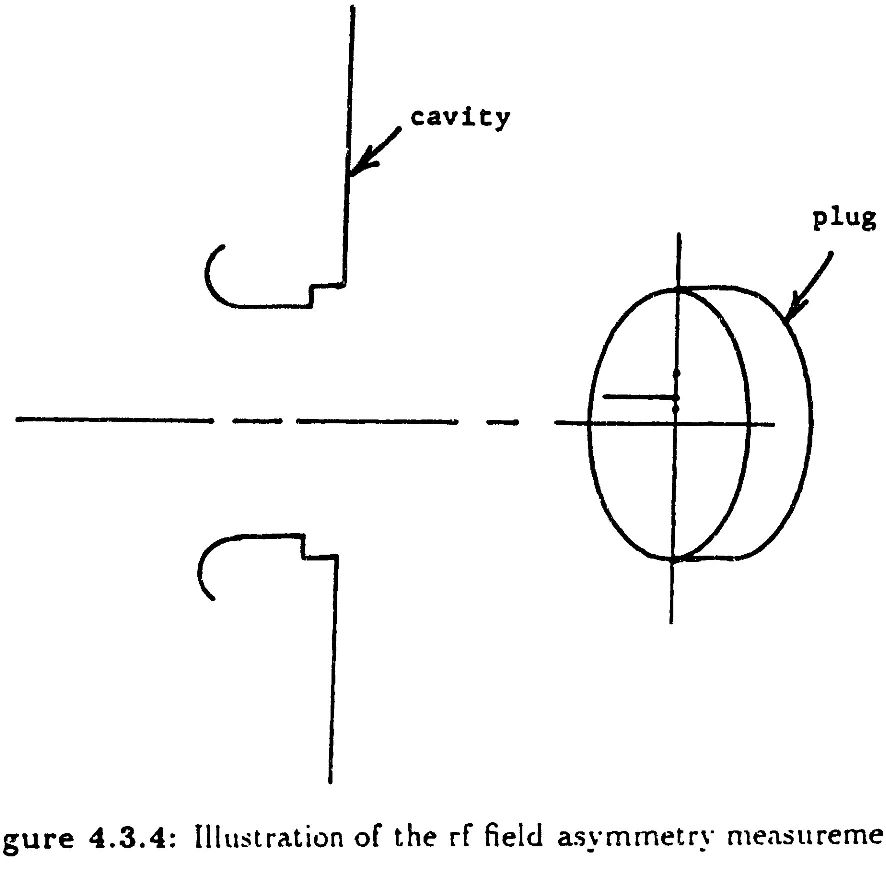

Figure 4.3.4: Illustration of the rf field asymmetry measurement setup.

were phase measurements. The reproducibility was only to within 0.5° which is much greater than the expected 0.05° deviation to be found from eq. (40), thus the phase contribution to particle deflection was not included in measurements.

D. Measurement Results

Listed in Table 4.3.1 is a sample series of resonant frequency measurements with successive 180° rotations of the pin indicating measurement reproducibility. Estimates of particle deflection, α ; offset, Δy ; bunch shear, $\Delta\alpha$; and rf center displacement, δy, are listed in Table 4.3.2 given the value of A from measurements performed at the three pin positions. A sample plot of the time evolution of these quantities is shown in Fig. 4.3.5 where the particle exits the cavity at $t = 120$ ps. Plotted in Fig. 4.3.6 are parameters of axial particle motion where the equivalent axial electric field was inferred from URMEL. The traveling wave contribution to transverse motion ($\Delta\phi$ in eq. (30) has not been included in these tables and figures. It would typically give a transverse kick of the same order as the dipole contribution.

From Table 4.3.2 the field asymmetry will contribute to the bunch's spacial spread $\Delta y \simeq 0.01$ mm, to bunch shear $\Delta\alpha \simeq 0.45$ mrad, and with $\gamma \sim 4$ exiting the gun, the added normalized bunch emittance will be $\Delta\epsilon_n \simeq 0.02$ mm·mrad. Compared to the expected normalized emittance of $\epsilon_n \simeq 420$ mm·mrad yielded from PARMELA, the field asymmetry contribution is negligible and a single rf feed will be used in the photo-cathode cavity.

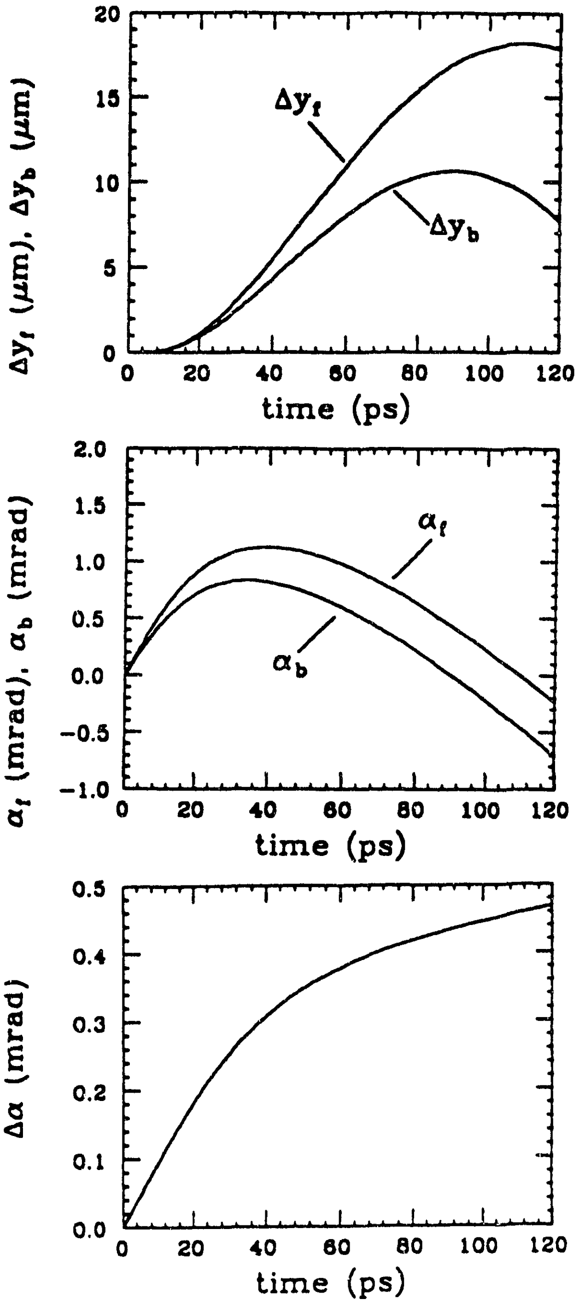

Figure 4.3.5: Time evolution of rf field asymmetry parameters: transverse offset Δy (top), particle deflection α (middle) and bunch shear $\Delta\alpha = \alpha_f - \alpha_b$ (bottom). Subscripts f and b refer to front and back of the bunch , respectively.

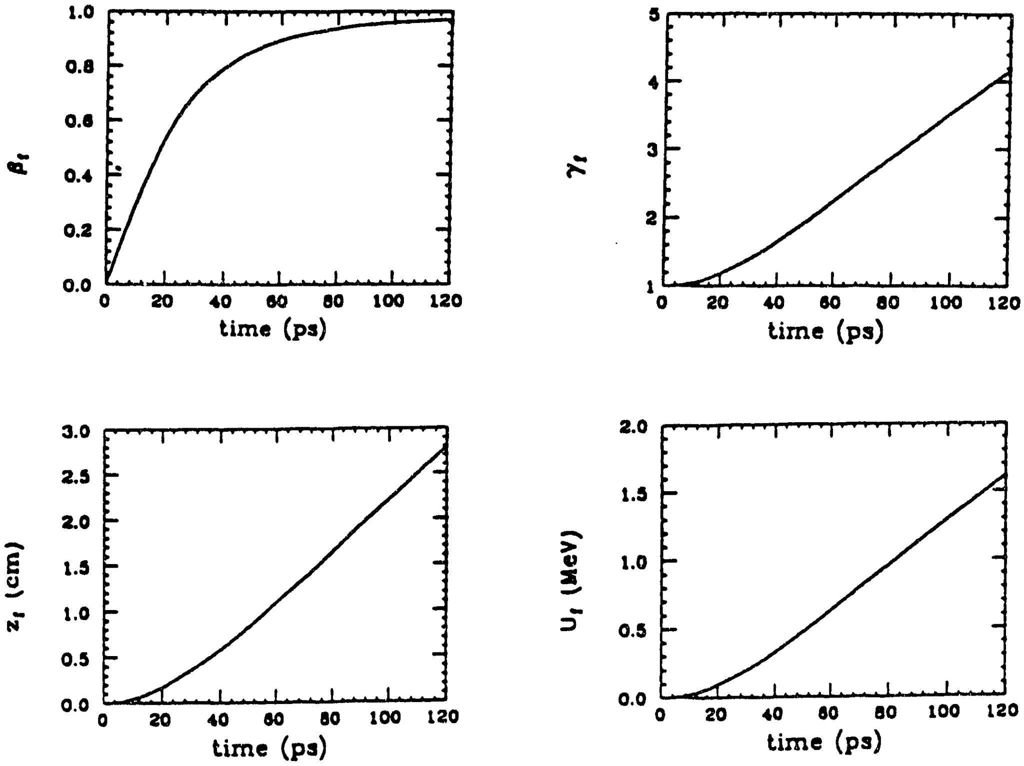

Figure 4.3.6: Time evolution of axial motion parameters: axial velocity β (upper left), axial position z (lower left), kinetic energy U (lower right) and γ (upper right).

Table 4.3.1: Frequency measurements for rf field asymmetry.

$\Delta\theta$ (degree)	f_1 (MHz)	$\Delta\theta$ (degree)	f_2 (MHz)
0	1301.757736	180	1301.789157
360	1301.764315	540	1301.804725
720	1301.769717	900	1301.797416
1080	1301.765101	1260	1301.782412
1440	1301.763947	1620	1301.791260
1800	1301.766640	1980	1301.801647

Table 4.3.2: Parameters for rf field asymmetry.

h (inch)	1/4	1/2	1
α_f (mrad)	−0.16	−0.29	−0.24
α_b (mrad)	−0.48	−0.85	−0.71
$\Delta\alpha$ (mrad)	0.315	0.56	0.47
Δy_f (μm)	12.0	21.3	17.9
Δy_b (μm)	5.1	9.1	7.6
δy (mm)	0.17	0.31	0.26

4.3.3 LASER SPOT ALIGNMENT

A. Simulation Approach

The effect on particle divergence and offset due to the laser spot asymmetrically illuminating the photo-cathode surface was treated by running PARMELA with the initial particle distribution at the photo-cathode surface shifted transversely by specified amounts. The random particle generator in PARMELA already creates distributions that are not perfectly symmetric, but the misalignment and divergence is vanishingly small and asymmetries on the order of a mesh size yield no relevant interpretation. In these simulations only the unperturbed TM_{0n} rf fields are present in the cavity, space charge forces are included, and an external magnetic field is applied. All of the physical quantities described in the following are mean values averaged over the entire bunch.

B. Simulation Results

In Table 4.3.3 are listed three initial particle distribution offsets, δy ; bunch offset exiting the photo-cathode cavity, Δy ; and bunch divergence exiting the photo-cathode cavity, α. The transverse kicks are nearly linear with initial distribution offset and the product $\beta\gamma\, \Delta y\, \alpha \simeq 1.6$ mm·mrad is about 0.4% of the expected normalized emittance *per 0.1 mm* of initial distribution offset (or laser misalignment). This displacement and divergence, however, is nearly uniform throughout the bunch and may be corrected with accelerator alignment and solenoidal focusing, i.e., they don't contribute to added emittance.

Table 4.3.3: Parameters for laser spot alignment.

δy (mm)	0.16	0.95	1.16
Δy (mm)	0.28	1.6	2.0
$\Delta y / \delta y$	1.75	1.68	1.72
α (mrad)	3.86	21	29
$\alpha / \delta y$ (mrad/mm)	24	22	25

4.4 HIGH POWER TESTS OF THE GUN CAVITY

4.4.1 INTRODUCTION

Recently, the electrical breakdown and discharges in vacuum under high gradient rf fields have been studied extensively.[59–61] Since our design of the gun cavity is based on a field gradient of 92 MV/m on the center of the photocathode and a peak surface field of 127 MV/m around nosecone with 1.5 MW input rf power, it is desirable to investigate the behavior of the gun cavity under such a high rf field. Before moving on to the experimental studies, we will describe some related physics here.

When an increasing rf field is applied to the cavity, a noticeable amount of current, called dark current or prebreakdown current, appears beginning from a certain level of applied field. An interesting feature of the dark current, I, is that its dependence on the surface electric field, E, when presented in a Fowler-Nordheim plot[62]: $\log_{10}(I/E^2) = f(1/E)$, often yields straight lines. Over the years, there have been several hypotheses on the mechanism of the rf breakdown in cavities. Field emission is one of the most popular theories. The field emission current, when flowing through a point on the cathode, causes the point to heat up, then melt and vaporize, and in the end leads to breakdown. Another more recent model is called Explosive Electron Emission.[63–65] According to this model, rf breakdown occurs when the field emission current density at some micro-protrusion site reaches around 10^8 to $10^9 \mathrm{A/cm}^2$ and raises the local temperature to the melting point. Instantaneous melting and evaporation of metal takes place and a local plasma discharge occurs. The entire event resembles a volcanic eruption.

Recently, Loew and Wang conducted a series of experiments to study the rf breakdown in room temperature electron linac structures.[66] They found an empirical formula for the electrical field breakdown limit which scales roughly as $E(\mathrm{MV/m}) \sim 195[f(\mathrm{GHz})]^{1/2}$. The breakdown limits predicted by this relation exceed the traditional Kilpatrick criterion,[67] $E(\mathrm{MV/m}) \times \exp(-4.25/E) = 24.7[f(\mathrm{GHz})]^{1/2}$, roughly by a factor of seven. This discrepancy is not too surprising since the Kilpatrick formula was based on a gap of parallel plates which is quite different from the conditions inside rf cavities with nose cones or irises. The maximum surface field attainable in our 1.3 GHz gun cavity is 222 MV/m according to Loew and Wang's formula.

4.4.2 EXPERIMENTAL SETUP

A schematic drawing of the gun cavity high power test configuration is shown in Fig. 4.4.1, while a photograph of the experimental setup is shown in Fig. 4.4.2. When these tests were performed, rf power was not available for the Argonne Wakefield Accelerator project. Therefore the experiment was set up in the linac of the Argonne Chemistry Division with a klystron being able to provide rf power of up to 6 MW which is more than enough for our planned input power of 1.5 MW. A portable stand made of unistruts and a wooden board was used to support the cavity and all the associated equipment. As seen in Fig. 4.4.1, the top of the cavity is connected to an input waveguide, a waveguide/vacuum window, and

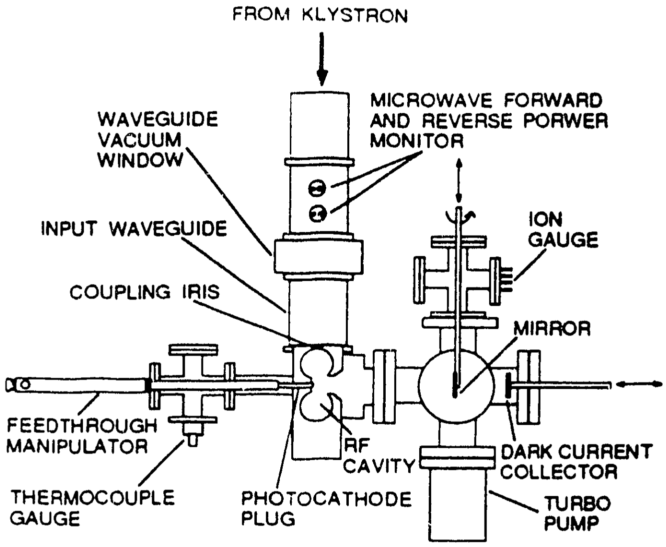

Figure 4.4.1: The schematic of the high power test.

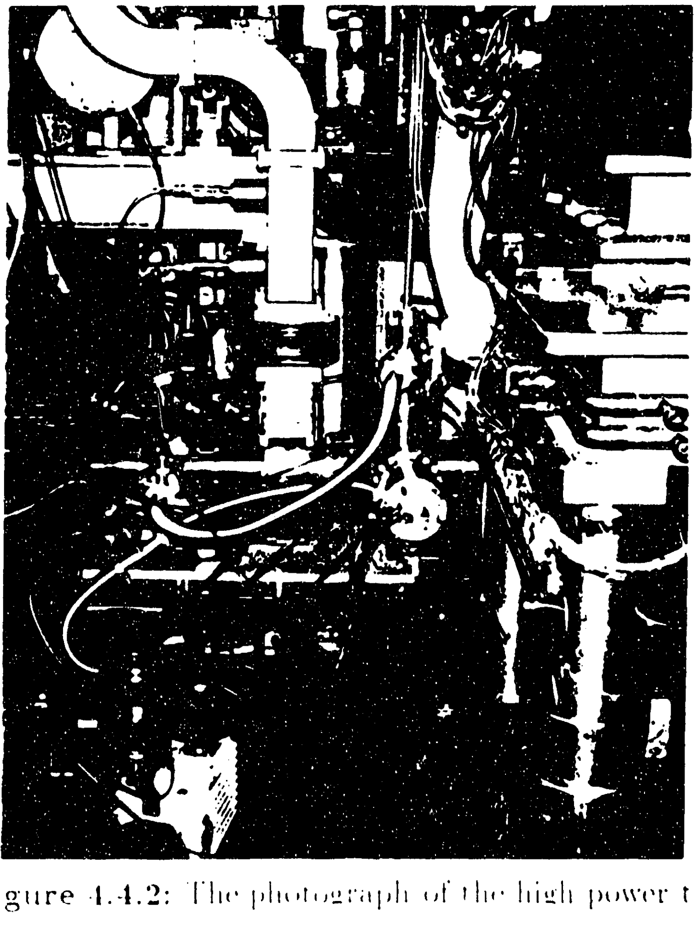

Figure 4.4.2: The photograph of the high power test.

another waveguide section with a forward and reverse rf power monitor. To the rear of the cavity is a linear motion feedthrough manipulator (Huntington, Model VF-159) with an increment resolution of 0.001 inch, connected to the copper photocathode plug through a 4-way vacuum cross for fine tuning of the resonant frequency. The major diagnostics of this experiment consist of a Faraday cup with high sensitivity phosphorescent screen (MCI optonix PFG) to monitor the dark current and beam position and a CCTV camera (Hitachi, Model HV-735U) with video recorder to view breakdown sparks. The Faraday cup is made of an aluminum disk of 3.5 inch diameter and 0.25 inch thick which is enough to stop the < 2 MeV dark current beam since the energy loss per unit distance in aluminum is 4.374 MeV/cm. These diagnostics were mounted in a 6-way cross of 4 inch inner diameter which is connected to the front of the cavity. Three ports of the 6-way cross were sealed with transparent acrylic plastic (Plexiglas) windows for viewing the sparks and handling the motions of the mirror and Faraday cup. A 4-way cross is on one port of the 6-way cross to hold an ion gauge and the front-surface mirror which is epoxied onto an aluminum rod. This mirror can be rotated to view the sparks within the cavity by the external TV camera. A turbomolecular pump (TURBOVAC TMP-150) with a roughing pump (TRIVAC "A" Dual Stage Rotary Vane Pump) is used in the front side of the cavity to produce a vacuum of about 10^{-6} Torr. The rear side of the cavity is pumped through a flexible pipe connected to the front side of the cavity.

The preparation and conditioning of the gun cavity is the main challenge of this experiment. After the first rough cut for the cavity shape, the copper was heat checked at 1800° F to make sure there are no residual gases remaining in the copper which results in blistering of the surface. Then the cavity surfaces were iteratively machined to make sure the resonant frequency of the cavity was steadily converging toward our design frequency of 1.3 GHz. The shape and size of the iris for coupling rf power into the cavity was machined to minimize the reflection coefficient, which is the ratio of reflected voltage to incident voltage. The cavity was then sent to an on-site optical polishing shop for a fine surface polish. The polishing work was done by hand with the cavity on a rotating table, using metrologist's cloths and grits down to one micron. The inner cavity surfaces achieved a near optical polish. The cavity components were brazed together in a dry hydrogen atmosphere. Three stages of brazing corresponding to three different melting temperatures of brazing alloys were used to allow the fabrication of various components. After brazing, the cavity was vacuum tested using a Helium leak detector and found to be Helium leak tight to better than $3 \cdot 10^{-8}$ standard c.c./sec. However it was found that the cavity resonant frequency had been shifted up by 1.8 MHz after brazing, probably due to material removal in the polishing process. To correct the frequency error, we used a precision press system to exert forces up to 8500 pounds on the central region of both sides of the cavity. A network analyzer and a force meter monitored the frequency and the force simultaneously to bring the resonant frequency down to our designed frequency which, as discussed previously, takes into account effects of frequency dependance on the operating temperature and pressure of the cavity.

Two separate directional couplers were used to distinguish between rf power transmitted in the forward and reverse directions with respect to the cavity. The coupling factors, which are defined as 10 $\log_{10}$(Output power/Input power) dB, for both directional couplers are -70 dB. The directivity, which is a measure of how well the rf power couples only to the desired direction, is > 30 dB. Two crystal detectors were used in conjunction with the directional couplers. The function of the crystal detector is to convert an rf signal from the directional coupler into a voltage which can be measured directly on an oscilloscope. The calibration of the crystal detector was performed by using a network analyzer (HP 8510A), an rf power meter (BOONTON 4200), and a voltage multimeter (HP E2377A). The calibration curve (rf power vs voltage) for one of crystal detectors is shown in Fig. 4.4.3. The rf power provided from the network analyzer is in the milliwatt range. Therefore, we used a 20 dB attenuator in addition to the -70 dB coupling from the directional coupler to bring the megawatt rf power waveguide signals down to measurable levels in the milliwatt range.

4.4.3 RESULTS AND DISCUSSIONS

The procedure of the experiment is as following. First, the resonant frequency of the cavity is tuned by moving the photocathode plug to match the frequency of the klystron. The frequency matching is obtained by observing when the dark current is maximized, and the cathode plug is then fixed at that position for the remainder of the experiment. A polaroid camera was used to take pictures from the oscilloscope for measurements of forward power, reverse power, and dark

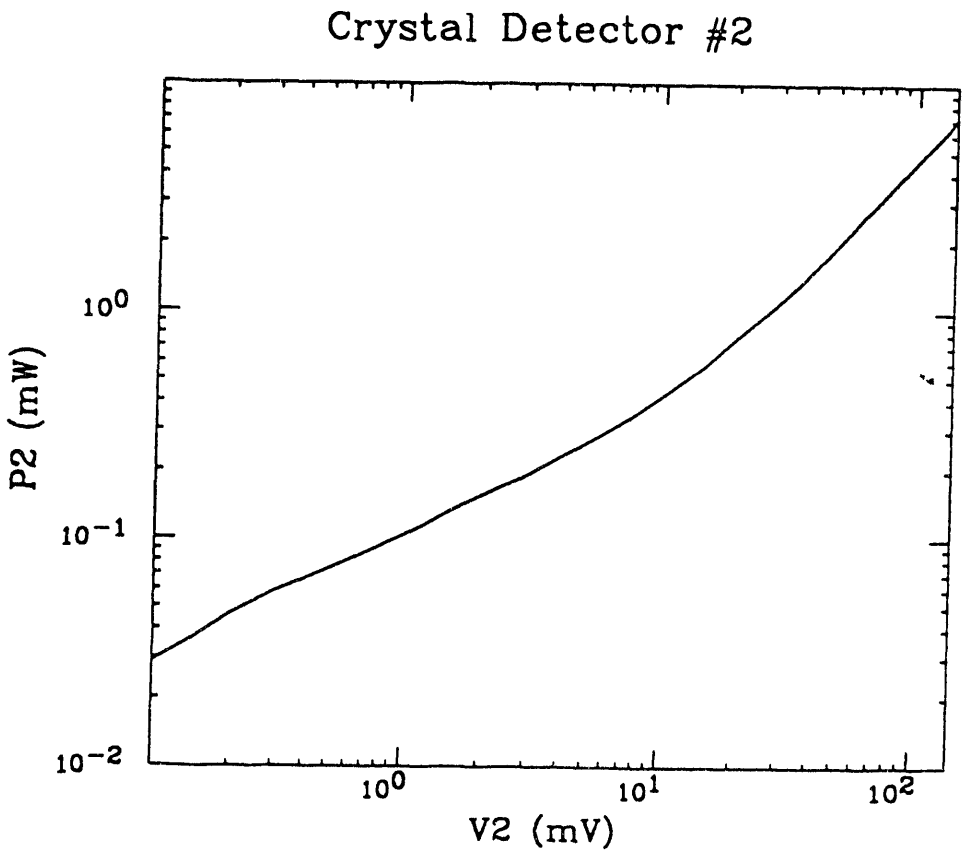

Figure 4.4.3: The calibration curve for a crystal detector.

current. A video cassette recorder recorded flashes and sparks viewed by the TV camera.

The rf pulsing of the cavity for about half an hour at each power level leads to surface cleaning through field emission bombardment and as a result of the removal of surface imperfections and impurities. This is observed as a gradual reduction in the dark current. The input resistance of the oscilloscope channel is 50 Ohm, therefore, the dark current at beginning of rf processing shown in Fig. 4.4.4 is around 400 mA (= (4 div · 5 V/div)/50 Ohm), while the dark current shown in Fig. 4.4.5 is about 40 mA. This is a reduction by a factor of ten after rf processing for 20 minutes at a 0.6 MW rf power level. As the dark current dwindles, the surface electric field increases as a result of less beam loading due to the dark current. This effect is manifested by the appearance of the sparks when the dark current drops down to some threshold level. The sparks drive an instantaneous surge of dark current which is followed by a steady decrease to another threshold level and arcing again. The threshold level very slowly decreases, improving the surface electric field where arcing occurs.

This pattern of arcing, subsequent recovery, and gradually increasing the rf power continued up to the maximum attainable field beyond which the sparks and flashes are almost continuous and spectacular. The maximum rf power level achieved for this experiment was 1.125 MW which corresponds to a surface electric field of 80 MV/m on the center of photocathode. This is 87% of our designed goal of 92 MV/m.

Figure 4.4.6 shows a typical picture of forward and reverse rf power crystal

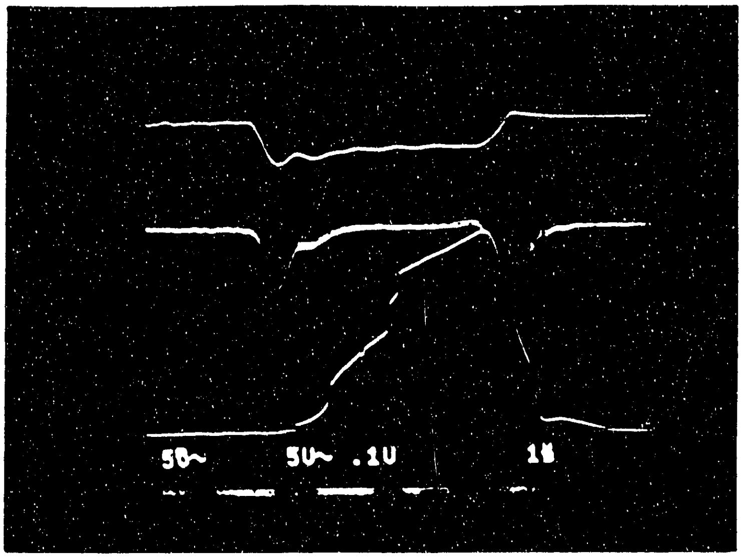

Figure 4.4.4: Oscilloscope traces at beginning of rf processing at 0.6 MW. Horizontal scale: time=1 μs/div. Vertical scales: forward power(top)=0.1 V/div. reverse power(middle)=5 mV/div. dark current(bottom)=5 V/div.

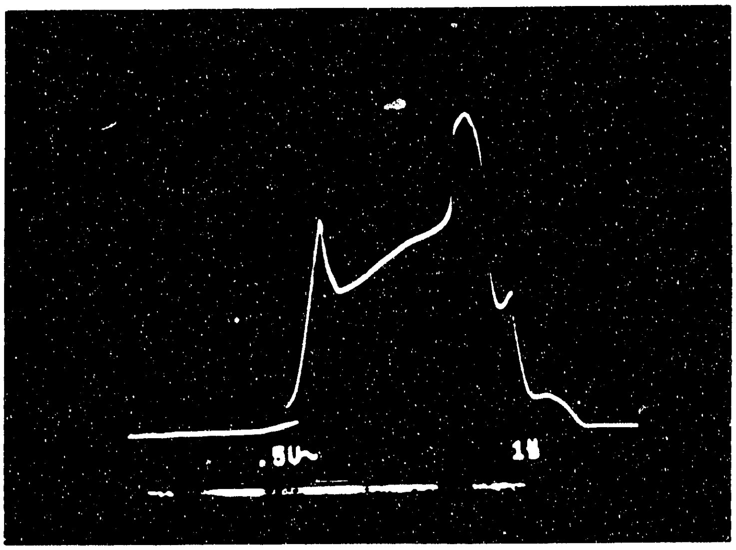

Figure 4.4.5: Oscilloscope traces after rf processing for 20 minutes at 0.6 MW. Horizontal scale: time=1 μs/div. Vertical scale: dark current=0.5 V/div.

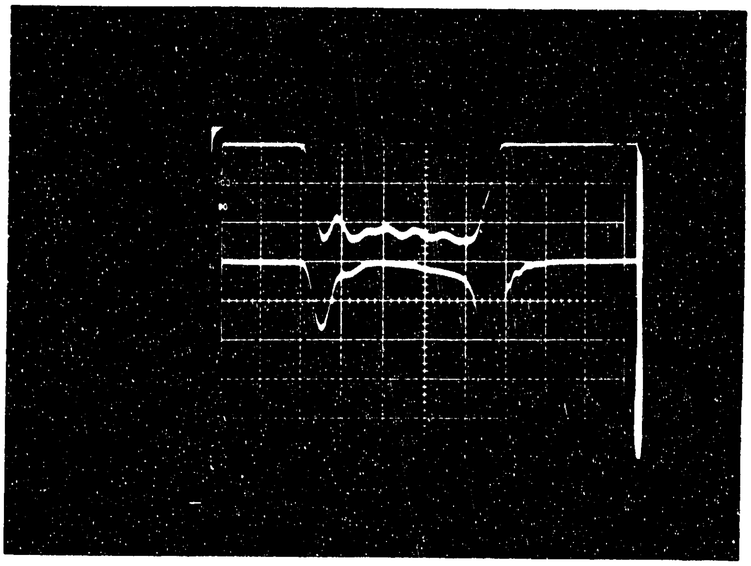

Figure 4.4.6: Oscilloscope traces at 1 MW rf power. Horizontal scale: time=1 μs/div. Vertical scales: forward power(top)=10 mV/div. reverse power(bottom)=10 mV/div.

detector signals. The top curve is the forward detector which is nominally at 20 mV, corresponding to about 1 MW of input rf power. The bottom curve indicates the reflected power which has an interesting two-spike feature. The first spike is due to the initial power build up inside the cavity. The second spike is due to the termination of the applied rf pulse which causes the steady-state rf energy in the cavity to dump to the external waveguide.

Let's make an estimate of the acceleration voltage decrement due to the beam loading by the dark current. With the acceleration phase chosen to maximize the kinetic energy, the beam energy at the exit of the gun cavity is about 2 MeV for 1.5 MW input power into the cavity as simulated by PARMELA. It is reasonable to assume the average beam energy of measured dark current, which can be emitted throughout one third of an rf-period,[61] is around 1 MeV. The dark current measured at the 1.125 MW power level is around 140 mA. The beam power can be calculated as 140 mA × 1 MV = 0.14 MW. This shows that the dark current has caused the input power to drop from 1.125 MW to 0.985 MW. Therefore, the electric field amplitude on the center of the photocathode is calculated to have reduced from 80 MV/m to 75 MV/m, a decrease of 6.2%.[68]

However, the cavity was not in optimal condition for the high power tests. The vacuum of the cavity was only $3 \cdot 10^{-6}$ Torr, whereas for the AWA project, the vacuum of the gun cavity is planned to reach 10^{-9} Torr. Also the inner surfaces of the cavity were not as well prepared as would be desirable. The best preparation would consist of a thorough chemical cleaning and then vacuum baking at 200°C to 250°C for more than 24 hours. Also, a longer period (at least one week) of rf processing which leads to surface cleaning is necessary. We believe if we do a better job of preparing the gun cavity in the future, the dark current should be highly reduced and the maximum attainable surface fields will be much improved.

5 Summary and Conclusions

The quest for more powerful high energy accelerators to continue the tour of probing fundamental laws of the nature leads to the investigation of the feasibility for building a very high gradient accelerator. The success of the proof-of-principle experiments at AATF demonstrated the wakefield acceleration is a promising scheme for future high energy linear accelerators.

To demonstrate a practical 1 GeV wakefield accelerator with an acceleration gradient of greater than 100 MV/m, the Argonne Wakefield Accelerator was proposed. We have presented the design studies for the phase-I of AWA. The major goal for phase-I is to generate the electron drive bunch with 100 nC charge and 10 ps bunch length. A laser photocathode rf gun cavity with very high electric fields on the cathode surface and a preaccelerator with very large iris were designed using the frequency-domain code URMEL. We have also measured cavity properties in a series of low rf power level bench tests. Good agreements were found between measurements and URMEL calculations.

Beam dynamics simulations for the gun and the preaccelerator were performed using particle-in-cell codes TBCI-SF and PARMELA. An optimized set of beam parameters which can be used in the operation of AWA was presented. The operational beam quality for AWA is comparable to that of AATF except the total charge is 100 nC/bunch for AWA instead $\sim$ 2 nC/bunch for AATF. The effect of sagitta for the curved beam was studied. We found the sagitta plays a subtle role in reducing the energy spread. However, the beam quality is a compromise among the bunch length, emittance, and total charge. We also studied the laser amplitude jitter effect and the laser timing jitter effect and found they should not be of serious concern for the normal operation of AWA.

We also measured the field asymmetry due to the rf coupling iris in the side wall of the cavity. We found the field asymmetry contribution to the normalized emittance is negligible and a single rf feed will be used. The laser spot misalignment problem was studied by PARMELA. The displacement and divergence due to misalignment are nearly uniform throughout the bunch and may be corrected with accelerator alignment and solenoidal focusing.

We also conducted high power tests for the gun cavity. An electric field of 80 MV/m on the center of cathode surface was achieved. This is 87% of our designed goal of 92 MV/m. However, the cavity was not in its optimal condition for the tests. The rf power will be available for the AWA in the near future and a much longer period of rf processing will definitely do a better job in conditioning the cavity. Also the vacuum condition will be much better for the AWA operation than for the test. We believe our design goal of 92 MV/m is achievable since it is far below the SLAC empirical limit.

In conclusion, through simulation results and preliminary experimental tests, we believe the generation of a high current, short pulse electron drive beam for the AWA operation can be achieved. This will lift the wakefield acceleration technology to a practical level for being a candidate for the future high energy accelerator.

References

1. Ya. B. Fainberg, in *Proc. CERN Symposium on High Accelerators and Pion Physics, Vol. 1* (Geneva, 1956), p. 84.
2. Ya. B. Fainberg, At. Energ. **6**, 431 (1959).
3. A. G. Ruggiero, in *Proc. 1986 Linear Accelerator Conf.* (Stanford, California, 1986), p. 549; SLAC-Report-303 (September, 1986).
4. A. G. Ruggiero, P. Schoessow, and J. Simpson, in *Advanced Accelerator Concepts*, edited by F. Mills, AIP Conf. Proc. 156 (American Institute of Physics, New York, 1987), p. 247.
5. P. Chen, J. M. Dawson, R. W. Huff, and T. Katsouleas, Phys. Rev. Lett. **54**, 693 (1985).
6. R. D. Ruth, A. W. Chao, P. L. Morton, and P. B. Wilson, Part. Accel. **17**, 171 (1985).
7. P. Chen and R. Ruth, in *Laser Acceleration of Particles*, edited by C. Joshi and T. Katsouleas, AIP Conf. Proc. 130 (American Institute of Physics, New York, 1985), p. 213.
8. R. Keinigs, M. E. Jones, and W. Gai, Part. Accel. **24**, 223 (1989).
9. R. Keinigs, W. Peter, and M. E. Jones, Phys. Fluids B **1**, 1872 (1989).
10. J. Simpson, J. Norem, P. Schoessow, F. Cole, and A. G. Ruggiero, IEEE Trans. Nucl. Sci. **NS-32**, 3492 (1985).

11. R. Konecny, J. MacLachlan, J. Norem, A. G. Ruggiero, P. Schoessow, and J. Simpson, in *Proc. 1986 Linear Accelerator Conf.* (Stanford, California, 1986), p. 434; SLAC-Report-303 (September, 1986).

12. H. Figueroa, W. Gai, R. Konecny, J. Norem, A. Ruggiero, P. Schoessow, and J. Simpson, Phys. Rev. Lett. **60**, 2144 (1988).

13. J. M. Dawson, "Plasma Particle Accelerators," Scientific American (March, 1989), p. 54.

14. Pisin Chen, Part. Accel. **20**, 171 (1987).

15. J. B. Rosenzweig, D. B. Cline, B. Cole, H. Figueroa, W. Gai, R. Konecny, J. Norem, P. Schoessow, and J. Simpson, Phys. Rev. Lett. **61**, 98 (1988).

16. J. B. Rosenzweig, P. Schoessow, B. Cole, W. Gai, R. Konecny, J. Norem, and J. Simpson, Phys. Rev. A **39**, 1586 (1989).

17. J. B. Rosenzweig, B. Cole, C. Ho, W. Gai, R. Konecny, S. Mtingwa, J. Norem, M. Rosing, P. Schoessow, and J. Simpson, Physica Scripta **T30**, 110 (1990).

18. J. B. Rosenzweig, P. Schoessow, B. Cole, C. Ho, W. Gai, R. Konecny, S. Mtingwa, J. Norem, M. Rosing, and J. Simpson, Phys. Fluids B **2**, 1376 (1990).

19. W. Gai, P. Schoessow, B. Cole, R. Konecny, J. Norem, J. Rosenzweig, and J. Simpson, Phys. Rev. Lett. **61**, 2756 (1988).

20. M. Rosing and W. Gai, Phys. Rev. D **42**, 1829 (1990).

21. E. Garate, Phys. Fluids B **3**, 1104 (1991).

22. J. Simpson, Argonne National Laboratory report No. ANL-HEP-WF-157 (November, 1990).

23. Wei Gai, Argonne National Laboratory report No. ANL-HEP-WF-159 (Feburary, 1991).

24. E. Chojnacki, W. Gai, C. Ho, R. Konecny, S. Mtingwa, J. Norem, M. Rosing, P. Schoessow, and J. Simpson, J. Appl. Phys. **69**, 6257 (1991).

25. Wei Gai and Ching-Hung Ho, J. Appl. Phys. **70**, 3955 (1991).

26. J. Simpson *et al.*, Argonne National Laboratory report No. ANL-HEP-TR-89-81 (April, 1990).

27. P. Schoessow, E. Chojnacki, W. Gai, C. Ho, R. Konecny, S. Mtingwa, J. Norem, M. Rosing and J. Simpson, in *Proc. 2nd European Particle Accelerator Conf.* (Nice, France, 1990), p. 606.

28. M. Rosing, E. Chojnacki, W. Gai, C. Ho, R. Konecny, S. Mtingwa, J. Norem, P. Schoessow, and J. Simpson, in *Conf. Record of the 1991 IEEE Particle Accelerator Conf.* (San Francisco, California, 1991), p. 555.

29. E. Chojnacki, W. Gai, P. Schoessow, and J. Simpson, in *Conf. Record of the 1991 IEEE Particle Accelerator Conf.* (San Francisco, California, 1991), p. 2557.

30. Wei Gai, in *Advanced Accelerator Concepts*, edited by C. Joshi, AIP Conf. Proc. 193 (American Institute of Physics, New York, 1989), p. 121.

31. J. Fraser, R. Sheffield, E. Gray, P. Giles, R. Springer and V. Loebs, in *Proc. 1987 IEEE Particle Accelerator Conf.* (Washington, D.C., 1987), edited by E. Lindstrom and L. Taylor (IEEE, New York, 1987), p. 1705.

32. R. Sheffield, in *Physics of Particle Accelerators*, edited by M. Month and M. Dienes, AIP Conf. Proc. 184 (American Institute of Physics, New York, 1989), p. 1500.

33. C. H. Ho, Bull. Am. Phys. Soc. **35**, 956 (1990).

34. C. H. Ho, Argonne National Laboratory report No. ANL-HEP-WF-143 (April, 1990).

35. T. Weiland, Nucl. Instrum. Methods **216**, 329 (1983).

36. U. Laustroer, U. van Rienen and T. Weiland, "URMEL and URMEL-T User Guide," DESY M-87-03 (1987).

37. K. Halbach and R. F. Holsinger, Part. Accel. **7**, 213 (1976).

38. M. Menzel and H. Stokes, "User's Guide for the POISSON/SUPERFISH Group of Codes," Los Alamos National Laboratory report No. LA-UR-87-115 (January, 1987).

39. J. Fischer and T. Srinivasan-Rao, private communication.

40. T. Weiland, DESY 82-015 (March, 1982).

41. T. Weiland, Nucl. Instrum. Methods **212**, 13 (1983).

42. G.A. Loew and R.B. Neal, in *Linear Accelerators*, edited by P. M. Lapostolle and A. L. Septier (North-Holland, Amsterdam, 1970), p. 69.

43. J. Simpson, Argonne National Laboratory report No. ANL-HEP-AGN-15 (October, 1991).

44. N. J. Diserens, IEEE Trans. Magn. **MAG-18**, 362 (1982).

45. Lloyd M. Young, in *Physics of Particle Accelerators*, edited by M. Month and M. Dienes, AIP Conf. Proc. 184 (American Institute of Physics, New York, 1989), p. 1245.

46. P. Schutt, W. Bialowons, F.-J. Decker, F. Ebeling, R. Wanzenberg, T. Weiland and Xiao Chengde, in *Linear Accelerator and Beam Optics Codes*, edited by C. Eminhizer, AIP Conf. Proc. 177 (American Institute of Physics, New York, 1988), p. 173.

47. A. P. Banford, *The Transport of Charged Particle Beams* (Spon Ltd., London, 1966), p. 134.

48. J. D. Lawson, *The Physics of Charged-Particle Beams*, 2nd ed. (Clarendon Press, Oxford, 1988), p. 34.

49. W. Gai, Argonne National Laboratory report No. ANL-HEP-WF-124 (August, 1989).

50. J. Simpson, private communication.

51. J. Norem and W. Gai, in *Conf. Record of the 1991 IEEE Particle Accelerator Conf.* (San Francisco, California, 1991), p. 1984.

52. L. Burnod, in *Linear Accelerators*, edited by P. M. Lapostolle and A. L. Septier (North-Holland, Amsterdam, 1970), p. 365.

53. *CRC Handbook of Chemistry and Physics*, 72nd ed., edited by D. R. Lide (CRC Press, Boca Raton, 1991-1992), p. 9-31.

54. G. A. Loew *et al.*, in *The Stanford Two-Mile Accelerator*, edited by R. B. Neal (W. A. Benjamin, New York, 1968), p. 146.

55. G. A. Loew and R. B. Neal, in *Linear Accelerators*, edited by P. M. Lapostolle and A. L. Septier (North-Holland, Amsterdam, 1970), p. 98.

56. G. A. Loew *et al.*, in *The Stanford Two-Mile Accelerator*, edited by R. B. Neal (W. A. Benjamin, New York, 1968), p. 134.

57. E. L. Ginzton, *Microwave Measurements* (McGraw-Hill, New York, 1957), p. 439.

58. A. M. Vetter and R. P. Friedman, in *Proc. 1988 Linear Accelerator Conf.* (Newport News, Virginia, 1988), p. 58.

59. G. A. Mesyats and D. I. Proskurovsky, *Pulsed Electrical Discharge in Vacuum* (Springer-Verlag, Berlin, 1989).

60. G. A. Loew and J. W. Wang, Part. Accel. **30**, 225 (1990).

61. R. Bossart, "Beam Loading of RF-Gun by Dark Current," CERN, CLIC Note 138 (April, 1991).

62. R. H. Fowler and L. W. Nordheim, Proc. R. Soc. London A. **119**, 173 (1928).

63. G. A. Mesyats, IEEE Trans. Elec. Insul., **EI-18**, 218 (1983).

64. E. A. Litvinov, IEEE Trans. Elec. Insul., **EI-20**, 683 (1985).

65. G. N. Fursey, IEEE Trans. Elec. Insul., **EI-20**, 659 (1985).

66. G. A. Loew and J. W. Wang, "RF Breakdown Studies in Room Temperature Electron Linac Structures," SLAC-PUB-4647 (May, 1988).

67. W. D. Kilpatrick, Rev. Sci. Instrum., **28**, 824 (1957)

68. C. H. Ho, Argonne National Laboratory report No. ANL-HEP-WF-167 (March, 1992).

END

DATE FILMED

2 /23/ 93